Detectability of satellites around directly imaged exoplanets and brown dwarfs

Cecilia Lazzoni[1,2,⋆] Silvano Desidera[2], Raffaele Gratton[2], Alice Zurlo[3,4,5], Dino Mesa[2] and Shrishmoy Ray[1]
[1]University of Exeter, Astrophysics Group, Physics Building, Stocker Road, Exeter, EX4 4QL, UK
[2]INAF – Osservatorio Astronomico di Padova, Vicolo dell'Osservatorio 5, I-35122, Padova, Italy
[3]Núcleo de Astronomía, Facultad de Ingeniería y Ciencias, Universidad Diego Portales, Av. Ejercito 441, Santiago, Chile
[4]Escuela de Ingeniería Industrial, Facultad de Ingeniería y Ciencias, Universidad Diego Portales, Av. Ejercito 441, Santiago, Chile
[5]Aix Marseille Univ, CNRS, LAM, Laboratoire d'Astrophysique de Marseille, Marseille, France

Accepted XXX. Received YYY; in original form ZZZ

ABSTRACT

Satellites around substellar companions are a heterogeneous class of objects with a variety of different formation histories. Focusing on potentially detectable satellites around exoplanets and brown dwarfs, we might expect to find objects belonging to two main populations: *planet-like* satellites similar to Titan or the Galileian Satellites - likely formed within the scope of core accretion; and *binary-like* objects, formed within different scenarios, such as disk instability. The properties of these potential satellites would be very different from each other. Additionally, we expect that their characterization would provide insightful information about the history of the system. This is particularly important for planets/brown dwarfs discovered via direct imaging (DI) with ambiguous origins. In this paper, we review different techniques, applied to DI planets/brown dwarfs, that can be used to discover such satellites. This was achieved by simulating a population of satellites around the exoplanet β Pic b, which served as a test case. For each simulated satellite, the amplitude of DI, radial velocity, transit and astrometric signals, with respect to the planet, were retrieved and compared with the detection limits of current and future instruments. Furthermore, we compiled a list of 38 substellar companions discovered via DI to give a preliminary estimate on the probability of finding satellites extracted from the two populations mentioned above, with different techniques. This simplified approach shows that detection of *planet-like* satellites, though not strictly impossible, is very improbable. On the other hand, detection of *binary-like* satellites is within the capabilities of current instrumentation.

Key words: planets and satellites: detection– techniques:high angular resolution, image processing, photometric, radial velocities

1 INTRODUCTION

In the past decade, the direct imaging (DI) technique has proven to be an invaluable method to investigate planetary systems. In fact, even if the indirect methods such as radial velocities (RV) and transits are more prolific in terms of the number of detections, substellar companions detected via direct imaging have the advantage of revealing simultaneously a plethora of information on the object. The combination of 8-meters size telescopes with the performances of extreme adaptive optics devices has provided precise measurements of the spectro-polarimetric characteristics of planets and brown dwarfs (e.g. HD206893 B Delorme et al. (2017); HR2562 B Konopacky et al. (2016); Mesa et al. (2018); GJ504 b Kuzuhara et al. (2013); HD95086 b Chauvin et al. (2018); PDS70 b Müller et al. (2018); 51 Eri b De Rosa et al. (2015); HIP65426 b Cheetham et al. (2019)) as well as precise measurements of their projected separation (∼ mas Maire et al. 2016b; De Rosa et al. 2020a). Multi-epoch observations of a single system allow for a precise determination of a part of the orbit or, in some cases, for a full characterization of the entire set of orbital parameters of the planet. This was for example the case for the planets of HR8799 (Zurlo et al. 2016; Wang et al. 2018; Gravity Collaboration et al. 2019; Goździewski & Migaszewski 2020) and β Pic b (Lagrange et al. 2019b).

In this paper we explore the possibility of detecting companions to brown dwarfs (BD) and planets discovered through DI. In fact, the physical characteristics of the latter are particularly suitable for the search of further bound objects (from now on, satellites) in their close vicinity, since they are relatively massive and usually with semi-major axis from tens to hundreds of au. Thus, their satellites can populate a wider area, identified by a large fraction of the Hill radius, around the planet. Similarly to planetary architecture, we may think of using a combination of different methods to explore the surrounding of an exoplanet for the presence of satellites, substituting the star as a reference with the planet itself as observational target. Each detection technique will be then limited to a specific portion of the parameters space.

This investigation is stimulated by the arrival of new instrumentation, both from space (e.g., MIRI/JWST, Danielski et al. 2018) and ground (e.g PCS/ELT Kasper et al. 2021), which will start a new era of the exoplanetary science, as well as by previous studies on the detectability of satellites with different techniques (see e.g. Heller 2016; Heller & Albrecht 2014; Vanderburg et al. 2018; Rodenbeck

⋆ E-mail: c.lazzoni@exeter.ac.uk

et al. 2020; Kipping et al. 2022). Even if we would be strongly biased towards the detection of massive satellites in the form of giant planets, these instruments might unveil cold worlds that are too faint to be directly detected at present times, including rocky planets and possibly the first exomoons. In addition to this, instruments constructed in the last few years (e.g., GRAVITY, Gravity Collaboration et al. 2017) allow or will soon allow (e.g., CRIRES+ especially with its link to SPHERE AO system, HiRISE; Otten et al. 2021; Vigan et al. 2022) dedicated characterization studies of directly imaged planets.

We notice that the term "moon" is usually dedicated to relatively small rocky bodies which orbit a planet, in analogy with the moons of our solar system. Here, instead, we will investigate a wider mass range of satellites, including objects similar in mass to the central planet, sometimes referred to as binary planets (Podsiadlowski et al. 2010; Ochiai et al. 2014).

Massive triple systems have already been discovered, such as the binary BD system that orbits around ϵ Indi (King et al. 2010) at a separation of 1500 au with masses in the range $[50, 70]$ M_{Jup}; the one around GJ 569 B (Femenía et al. 2011) at a separation of ~ 90 au and masses in the range $[55, 75]$ M_{Jup}; and a few other examples such as the pairs of BDs discovered around GJ 417 B (Kirkpatrick et al. 2001), HD130948 B (Potter et al. 2002) and AB Dor Ca/Cb (via interferometry, Climent et al. 2019). Thus, multiple systems, as exotic as they seem at first glance, are not a remote possibility to be investigated and might extend to smaller masses in the planetary regime.

More recently, the first detections of planetary-like satellites were claimed, as in the case of the Neptune-like candidate exomoon detected around the Jupiter-like planet Kepler 1625 B (Teachey & Kipping 2018), the 2.6 $M_\oplus$ candidate satellite for Kepler1708 b (Kipping et al. 2022) and the candidate companion (~ 1 M_{Jup}) around the low-mass (~ 10 M_{Jup}) brown dwarf DH Tau B (Lazzoni, C. et al. 2018). Though the existence of these candidates is debated (see e.g. Rodenbeck et al. 2018; Heller et al. 2019; Kreidberg et al. 2019) in each case, the ratio between the mass of the satellite and the planet q_s is quite high (0.01, 0.003 and 0.1 respectively) with respect to the solar system's moons which orbit giant planets (where the highest ratio, $q_s = 2.37 \times 10^{-4}$, is reached by Saturn's moon Titan). This might open up to a much more variegated spectrum (both in mass, separation and formation mechanisms) of satellites around exoplanets.

At the same time, from the properties of the satellites, we might extract useful insights on the formation mechanisms of directly imaged exoplanets and brown dwarfs. In fact, the formation mechanism of the latter is not very clear and likely involves core accretion (Mizuno 1980), disk instability/fragmentation (Cameron 1978; Boss 1997), and cloud/filament fragmentation (Larson 1985). Therefore, we can expect that different formation mechanisms deeply shape the properties of putative satellite companions.

The purpose of this work, then, is to explore the hunting capabilities of techniques such as RV, transits, astrometry and direct imaging, applied to imaged exoplanets and brown dwarfs. The latter, coupled with the best performing present and future instruments, could ultimately result in the detection of satellites of directly imaged companions.

We discuss in Section 2 the scenario for formation of satellites. In Section 3, we analyze the amplitudes of the signals (DI, RV, Transits and Astrometry) generated by a population of satellites around a test planet detected by direct imaging. In Section 4, we provide order of magnitude estimates of the probability of finding satellites to known planets discovered by DI using the various techniques for two different populations of satellites, that might be expected within different scenarios for planet formation. Finally in Section 5, we present a brief summary of the paper.

2 EXOMOONS AND BINARY PLANETS

The satellite category includes a huge variety of objects. In the Solar System, moons of the outer planets are often divided into two distinct classes: the regular and irregular satellites. The regular satellites orbit close to their host planet, moving on prograde orbits, with low inclinations (with respect to the planet's equatorial plane) and eccentricities (Mosqueira & Estrada 2003a,b; Sasaki et al. 2010). The irregular satellites, on the contrary, are scattered around their host planets and move on either prograde or retrograde orbits (Nesvorný et al. 2003; Jewitt & Haghighipour 2007; Holt et al. 2018), which are often highly inclined and eccentric. These moons are also typically relatively small (with the exception of Triton, the giant satellite of Neptune).

Due to their variety in mass and orbital parameters, multiple models have been proposed for planetary moon formation, and similar mechanisms can be adopted, in principle, to form extrasolar satellites. For the regular satellites of the giant planets, current theories suggest that during the phase of gas accretion, these planets developed their own small sub-nebulae, within which the satellites formed, similarly to the terrestrial planets within the main proto-planetary nebula (Canup & Ward 2002, 2006; Nesvorný et al. 2002; Mosqueira & Estrada 2003a,b; Mosqueira et al. 2010; Sasaki et al. 2010). The irregular satellites, on the other hand, are thought to have been formed elsewhere and then been captured, either through collisions (Goldreich et al. 1989; Woolfson 1999; Koch & Hansen 2011), three-body encounters between the host planet and binary planetesimals (Agnor & Hamilton 2006; Vokrouhlický et al. 2008), three-body encounters involving two of the giant planets and the captured object (Nesvorný et al. 2007), or through gas-drag (Ćuk & Burns 2004). Possibly a similar mechanism can be invoked also for the Pluto-Charon system (see e.g. Rozner et al. 2020, though the usual explanation for this system is giant impact, McKinnon 1989; Canup 2005; note, however, that Pluto is a dwarf planet). No mechanism is sufficient to explain all the observed properties of all irregular satellites (Jewitt & Haghighipour 2007), and so these objects are thought to be representative of the different processes that occurred during the final stages of planetary formation. The Moon is different, since it has formed when the young Earth was involved in a giant collision with a Mars-sized embryo, towards the latter stages of its accretion (Cameron & Ward 1976; Canup 2004; Benz et al. 1986; Reufer et al. 2012).

All moons in the Solar System have very small masses compared with their planets. Among the regular satellites of the giant planets, the highest value for the satellite mass ratio q_s is that of Saturn to Titan ($q_s = 2.37 \times 10^{-4}$). A much higher value of q_s is obtained for the Earth-Moon system ($q_s = 0.011$), with an extreme value of $q_s \sim 0.12$ for the Pluto-Charon system; in this last case the barycenter of the system lies out of the main body.

In relation to the planet formation channels, the lack of giant satellites is expected for a wide variety of planetary systems, being likely a consequence of formation in a core accretion scenario (see e.g. Canup & Ward 2002, 2006; Sasaki et al. 2010). However, planets may possibly form through other mechanisms - such as cloud fragmentation and disk gravitational instability - different from core accretion and for which the formation of giant satellites (or binary planets) is possibly not precluded. For instance, Inderbitzi et al. (2020) considered the formation of satellites in circumplanetary disks around a 10 M_{Jup} planet formed by gravitational instability at 50 au from its parent star

and found that, under favorable circumstances, a satellite as large as 10 $M_\oplus$ might form; this is close to the minimum mass required for runaway accretion. As already mentioned, a few candidate planetary satellites have already been claimed (Kepler 1625 b, Kepler 1708 b and DH Tau B). Somewhat relevant for the present discussion are also the discoveries of close brown dwarf-brown dwarf pairs in wide orbits around stellar hosts (e.g., King et al. 2010; Femenía et al. 2011; Kirkpatrick et al. 2001; Potter et al. 2002) and of isolated brown dwarf-planet pairs (e.g., Luhman et al. 2007; Chauvin et al. 2004a). As we will discuss in next Sections, the detection of giant satellites with $q_s > 0.1$ around massive planets or brown dwarfs appears possibly feasible, though difficult, at present with different techniques. If this were true, the possible discovery of giant satellites will shed light on the mechanisms of formation of their planets.

3 TECHNIQUES

To show which effects are produced by satellites orbiting a planet or a brown dwarf, including both the population of *planet-like* and *binary-like* satellites that we will introduce in Section 4, we chose a test system with a directly imaged companion, β Pic (Lagrange et al. 2010). β Pic b is, under many aspects, an instructive candidate for these kind of simulations thanks to its relatively small distance from the Sun (19.4 pc, Van Leeuwen 2007), its favorable contrast with respect to the central star, the edge-on configuration of the system (which increases the chances of detection with techniques such as RV and transits) and its dense coverage of observations taken in the past decade. The main parameters for β Pic b are listed in Table 1. The companion is a 12.8 M_{Jup} planet, as obtained by converting its contrast with respect to the central star (10^{-4} at 1.593 μm Lazzoni, C. et al. 2020b) with the BEX-COND-warm models (Marleau et al. 2019), using an estimated age of 16 Myrs (Desidera et al. 2021). Thanks to observations taken during a time interval spanning over 12 years, the orbit of the planet is well constrained with a semi-major axis of 8.9 au, an eccentricity of 0.01 (Lagrange et al. 2019b) and a Hill radius of $\sim$ 1.2 au. In the next sections we show the results that we obtained with the various detection techniques for a population of satellites injected around β Pic b.

The population of satellites that we simulated has masses in the range $[0.001, 1]M_P$, where M_P is the mass of the planet, with log-steps of 0.01 M_{Jup}. Considering this mass range, we take into account objects starting from the sub-earth mass regime up to binary systems with mass ratio 1. We considered only prograde circular orbits, coplanar with orbital plane of the planet, with semi-major axes in the range $[R_{Roche}, R_H/2]$, at log-steps of 0.0005 au, where R_H is the Hill radius of the planet (Raymond 2015). The $R_H/2$ limit for stable orbits was adopted following the results published by Domingos et al. (2006) whereas the inner boundary for stability is determined by the Roche limit, which determines the minimum separation possible for a satellite before the tidal disrupting due to the planet would break it up. The Roche limit is defined by the following equation

$$R_{Roche} = R_s \left(\frac{2M_P}{m_s} \right)^{1/3}, \quad (1)$$

where R_s and m_s are the radius and mass of the satellite, respectively, and R_s was calculated as described in Section 3.3, using (4).
Note that the detection techniques that we will discuss in the following are applied to the planet β Pic b itself, and not to the central star.

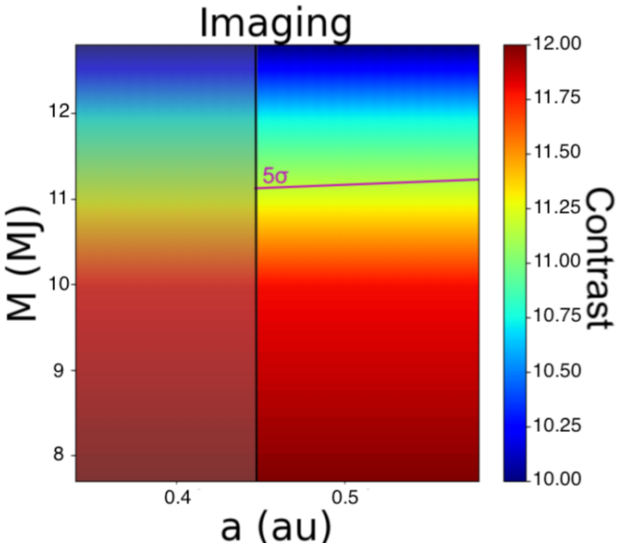

Figure 1. Contrasts with respect to the star related to a population of self-luminous satellites generated around β Pic b. The pink line represents the detection limits at 5σ level around the planet; the shaded area corresponds to the blind area around the planet within 1/2 FWHM

3.1 Direct Imaging

We generated a population of satellites with magnitudes in the range $[Mag_P, Mag_P + 2]$, where Mag_P is the H-band contrast in magnitude of the planet with respect to the star. Each absolute magnitude was then converted into mass using the age of the system and the BEX-COND-warm models (Marleau et al. 2019). Results are shown in Figure 1, where the shaded region represents the inaccessible area limited by half of the full width at half maximum (FWHM) of the PSF of the planet and contrast are given with respect to the star. Note also that this is the only technique for which we needed to plot the results using linear scales on both axis. In fact, the parameter space for DI is much smaller than the RV, transits or astrometry parameter spaces, for which, instead, we used logarithmic scales..

The 5σ level contrast curve shown in pink was derived following the procedure presented in Lazzoni, C. et al. (2018), thus carefully subtracting the contribution of the PSF of the planet with dedicated tools and then calculating the standard deviation in concentric annuli with a width of one FWHM each, starting from a separation of 1/2 FWHM from the center. This technique was already applied to the entire sample of substellar objects observed with SPHERE, leading to the discovery of a candidate companion around the low-mass brown dwarf DH Tau B.

In Lazzoni, C. et al. (2018) we analyzed a collection of 27 substellar companions detected with SPHERE, which is far from being a complete sample. First of all, we had to discard a few systems that were observed in poor weather conditions with resulting low-quality data sets. Also, two of the stars were close visual binaries and we had to exclude those systems from the analysis because we had no proper model PSF for the subtraction. For this kind of situation, an efficient solution could be the Reference Differential Imaging (RDI, Lafrenière et al. 2009), where a star, similar in magnitude and declination to the parent star of the system, is observed in a range of time very close to the coronagraphic observation (or even during the latter with a technique called star hopping, Wahhaj et al. 2021).

Moreover, the sample could be completed with objects that are

outside IRDIS/SPHERE FoV and will be reachable with instruments such as the Enhanced Resolution Imager and Spectrograph (ERIS, Kenworthy et al. 2018) which has a FoV of 54" × 54" and with targets which are observable only in the Northern hemisphere, using, for example the LBT facility, which will soon be equipped with a high contrast imager in the near infra-red, SHARK-NIR (Farinato et al. 2015).

Nevertheless, the SPHERE data analyzed so far let emerge the limitation of the technique due to: (i) the strong influence of the presence of the atmosphere, which can cause strong variations of the PSF during the observation and, in turn, unreliable features in the residuals of the object; (ii) and to the contrast reachable, which limit us to Jupiter-like objects. The next generation of instruments, both from ground and space, will overcome these problems. In fact, JWST/MIRI is expected to provide high-contrast imaging in the spectral range [5.6,28.8] μm, with expected contrasts from 10^{-4} to 10^{-6} at separations > 2 arcsec (Danielski et al. 2018). Even if the contrast were less deep than what is achievable with SPHERE, JWST/MIRI will be more efficient for colder and smaller objects due to the longer wavelengths coverage and the much better stability of the PSF over time with respect to ground-based observations. This will guarantee the reality of any detectable feature around the companion. Another limitation of this instrument is the dimension of the PSF that increases for increasing wavelengths and limits the detection of satellites at small separations. For example, for a planet like β Pic b, at the shortest wavelength available with MIRI, the FWHM of the PSF is ∼ 3.5 au, which is well beyond the Hill radius of the planet.

On the ground-instrumentation side, METIS on ELT (Brandl et al. 2010) will be able to access science cases similar to the ones presented for SPHERE, even if it is in the mid-infrared. This is due to the fact that the angular resolutions for the two instruments are roughly similar. However, with METIS we will have not only a gain in contrast towards less luminous planets but also a much higher quality of the observations. On even larger timescales, a dedicated high-contrast imager such as PCS on ELT (Kasper et al. 2021) is expected to reach contrasts of 10^{-8} at 30 mas and even deeper contrasts (∼ 10^{-9}) at larger separations. In the near-IR, though, we are limited once more to the detection of massive satellites which, at young ages, still emit at thermal wavelengths.

3.2 Radial Velocities

The amplitude of the motion of the planet in the radial direction due to the presence of a satellite was calculated using the equation given by Wright (2018), substituting the parameters of the star with the parameters of the planet, and the ones of the planet in the original expression with the parameters of the satellite. We thus obtain

$$K = \frac{m_s \sin i_s}{M_P} \sqrt{\frac{GM_P}{a_s}} \frac{km}{s * 1000} \quad (2)$$

where m_s and a_s are the mass and the semi-major axis of the satellite and i_s is the inclination of the satellite with respect to the plane of the planet. For the following discussion, we will consider the satellite being co-planar with the planet ($i = 90°$).

As shown in Figure 2, RV amplitudes of a few hundred of m/s are already reachable for the smallest satellites with masses $\lesssim 0.05$ M_{Jup}, if placed within 0.01 AU. We note, however, that this is an optimistic estimation given the favorable configuration considered. If the planet-satellite system is not aligned, the RV signal generated differs significantly from case to case. For example, a co-planar satellite of 0.05 M_{Jup} at 0.01 au gives an RV signal of 0.14 km/s

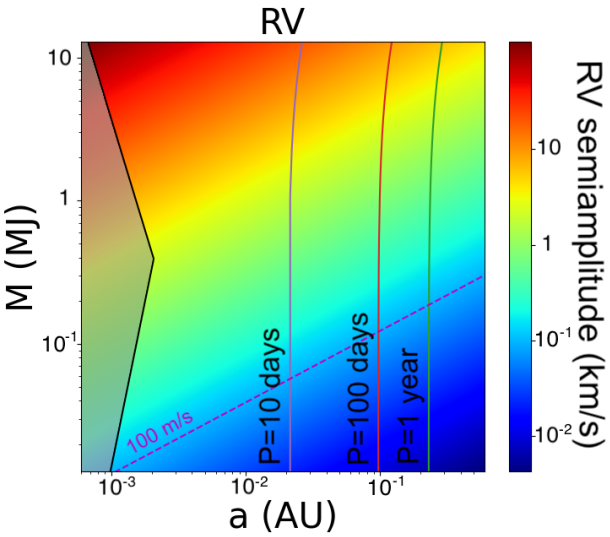

Figure 2. Radial velocity signals related to a population of satellites generated around β Pic b. The orbital periods are represented with purple (10 days), red (100 days) and green (1 year) curves and the Roche limits for tidal disruption is shown in black. The pink dashed line represents the detection limits achievable with HiRISE. The shaded grey area corresponds to the tidal disruption region.

whereas the same object on an inclined orbit of 20° produces K = 0.05 km/s, which would be not detectable.

The measurement of the RV of a directly imaged planet first has to face the issue of properly isolating the light of the planet itself from the bright halo of the central star. Therefore, it is mandatory to couple the spectrograph with an AO module. First efforts were already performed on some single-epoch measurements taken with CRIRES/VLT of β Pic b (Snellen et al. 2014) and GQ Lup B (Schwarz et al. 2016) and measurements taken with NIRSPEC/Keck of DH Tau B (Xuan et al. 2020) and HR8799 b and c (Ruffio et al. 2019). From these first tentative characterizations, it emerged how the detection of variations in RV signals of planets is not only strongly limited by the low photon-noise ratio but also by the contamination of the central star.

The intrinsic variability of planetary RV signals due, for example, to the presence of clouds in the atmosphere, to the accretion of material from the surrounding environment or to the orbit of the planet around the star, should be taken into account as well in such analyses and possibly identified through multi-epoch observations.

Vanderburg et al. (2018) presented a detailed description of the RV signal generated by the candidate exomoon of Kepler-1625 b and detection feasibility of a similar exomoon around directly imaged planets with current and future instruments. They consider, besides the Doppler signal due to orbital motion of the satellite around the planet and the planet around the star, the effects of partial planet illumination, of activity or heterogeneous cloud coverage, the light contribution of the exomoon with respect to the planet (peak-pulling), and the partial occultation by disk clumps. Therefore, we do not repeat here their evaluations and rather focus our attention on improvements thanks to forthcoming instruments.

In fact, relevant advances with respect to the early single-epoch attempts mentioned above can be obtained with updated instruments as CRIRES+ (Follert et al. 2014) and even more when this is coupled with the extreme-AO system of SPHERE as conceived with HiRISE

(Otten et al. 2021; Vigan et al. 2022). As shown in Figure 9 of Vigan et al. (2018), with HiRISE we expect contamination as small as a few 10^{-4} for a planet like β Pic b.

To estimate the typical accuracy achievable in the measures of a planet RV signal with an instrument such as CRIRES+, we considered the following steps. Using the Exposure Time Calculator (ETC: https://etc.eso.org/observing/etc/crires) the expected signal-to-noise ratio (SNR) in the H-band on β Pic b with CRIRES+ is about 40 per pixel in 1 hr (with 6×600 sec DITs) using the natural guide star adaptive optics (AO) on the primary. However, in this mode the dominant source of noise for β Pic b should be the stellar background. The latter is efficiently removed using HiRISE, which, however, is not currently included in the ETC. It should be noted that HiRISE will be less transmitting than the direct train to CRIRES+ (with the AO) by a factor of about 15 - though this is partly offset by the three times higher Strehl provided by the Sphere Ao for eXoplanet Observation (SAXO Fusco et al. 2016) of SPHERE with respect to Multi-Application Curvature Adaptive Optics (MACAO Paufique et al. 2006) available for CRIRES+.

We simulate this lower efficiency considering an object with H=15.5, rather than H=13.8. The SNR per pixel in this condition is about 10. To transform this into an error in RV, we may consider the observations of the late M-star TW Hya made by Figueira et al. (2010) where an internal accuracy of 6 m/s was obtained from spectra with SNR∼230 (this value has been traced back using the ETC, considering the stellar magnitude, the observing mode, DIT and number of exposures). Ignoring the much larger wavelength coverage of CRIRES+ with respect to CRIRES, the expected RV accuracy depends on the inverse of SNR and then observations with a SNR=10 for a late M-object (as β Pic b) should then be $\sim$ 140 m/s, but it can well be a factor of 1.5 better considering the much wider spectral range. We then assume an error of 85 m/s in 1 hr observation on β Pic b. Incidentally, if the lines of the planet and the satellite are not blended, detection of the RV variations from the satellite will provide a direct determination of the mass of the planet, crucial in modelling young objects.

We can then set a maximum detectable amplitude at $\sim$ 100 m/s (highlighted by a pink dashed line in Figure 2). We note that this threshold is based on the analysis with CRIRES of very late type stars (M5 and later), with spectra similar to those of bright DI exoplanets/BDs considered in this paper. Thus, on the one hand, the threshold obtained could result in an underestimate of detection capabilities, given the larger spectral coverage of CRIRES+. On the other hand, some substellar companions in the sample here have L/T spectral types, implying that the radial velocity signal is different from the one actually adopted. Even if the maximum detectable amplitude of $\sim$ 100 m/s is quite optimistic for actual instrumentation, it is quite realistic for HiRISE. In the β Pic b system this limit, together with the orbital period of the injected object around the planet, strongly constrains the characteristics of detectable satellites. Periods from 10 days to 1 year are plotted as vertical lines. At wider semi-major axis the orbital period increases, and, in turn, the probability of a detection drastically decreases.

A possible caveat to this technique, which is shared by transits and astrometry as well, is the time series of observation needed for the detection of a satellite. To improve the detection limits, several observations with top-class instrumentation on 8m telescopes are needed and this could be significantly time consuming, limiting the number of substellar objects that could be investigated.

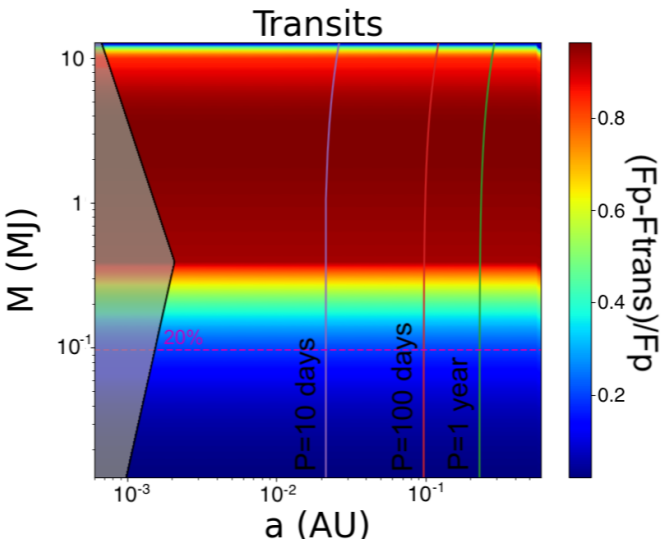

Figure 3. Transit signals related to a population of satellites generated around β Pic b. The orbital periods are represented with purple (10 days), red (100 days) and green (1 year) curves and the Roche limits for tidal disruption is shown in black. The pink dashed line represents the detection limits achievable with SPHERE. The shaded grey area corresponds to the tidal disruption region.

3.3 Transits

As mentioned above, the masses of the population of satellites generated around β Pic b vary from one-thousandth of the mass of the planet, thus $\sim$ 0.012 M_{Jup} $\sim$ 3.8 $M_\oplus$, to the mass of the planet itself. From both theoretical and observational studies we know that the radius of a planetary object tends to increase with its mass up to a limiting value (here we adopt 0.39 M_{Jup} following Bashi et al. 2017). For larger masses, instead, the radius settles roughly at 1 R_{Jup}, with a much slower increasing rate with respect to the mass. Since there is yet no study providing a mass *vs.* radius relation for satellites (either rocky or giants ones), we will adopt for the latter Eq (4). This is likely a good approximation because of the similar steps which take to the formation of both satellites (either within the circumplanetary disk or within the circumstellar disk and subsequent capture) and planets. The interactions between the primary object and the satellite (e.g. inflation of the latter due to heating caused by tidal locking) might cause deviations from the mass *vs.* radius relation adopted for satellites, but such an accurate analysis is beyond the general purposes of this paper.

Following the previous discussion, giant satellites are expected to have radii which are comparable with the radius of β Pic b itself. Thus, these objects could potentially completely obscure the primary planet. However, with increasing mass, a non-negligible contribution to the observed flux might come from the satellite itself. In fact, young giants are expected to be self-luminous so that a transiting massive satellite will cause a flux modulation more than an eclipsing transit, similarly to a binary star flux modulation.

In order to take into account these effects, we first consider the satellite as an obscurer, calculating the dimming in the flux following the equation (Seager & Mallen-Ornelas 2002)

$$\frac{F_P - F_{trans}}{F_P} = \frac{R_s^2}{R_P^2} \quad (3)$$

where R_P and R_s are the planet and satellite radii, respectively. As mentioned before, the radii are calculated with the relations given by Bashi et al. (2017)[1]

$$R = \begin{cases} 129362 \cdot \left(\frac{m_s}{M_{\rm Jup}}\right)^{0.55} km & \text{if } m_s < 0.39 M_{\rm Jup} \\ 77818 \cdot \left(\frac{m_s}{M_{\rm Jup}}\right)^{0.01} km & \text{if } m_s > 0.39 M_{\rm Jup} \end{cases} \quad (4)$$

Then, the contribution to the total flux given by the satellite is added to take into account its self-luminosity. This is done, only for satellites more massive than 0.2 M_{Jup} because the BEX-COND-warm models (Marleau et al. 2019), considered for the mass-luminosity conversion, are not available below that value (Linder et al. 2019). This is not a drastic issue since the self-luminosity of planets drastically decreases with the mass and the contribution to the flux below 0.5 M_{Jup} is negligible.

We show in Figure 3 the results obtained for the population of transiting satellites injected around β Pic b. Given the nearly edge-on configuration of the latter ($i = 89°$), the injected population of satellites, coplanar with the orbital plane of the β Pic b, will transit with good approximation through the center of the planet. We will discuss at the end of this Section the influence of the inclination on the detectability of satellites.

As shown in Figure 3, the limit for a detectable occultation/modulation for an instrument provided of an AO system is set at a 20% diminishing of the flux of the planet (following the discussion presented in Biller et al. 2021). This is justified by a combination of photometric precision reachable by AO instruments, which are mainly limited by variation of the observational parameters, and intrinsic variability due, for example, to the presence of clouds in the atmosphere. This implies that putative satellites around β Pic b with masses < 0.1 M_{Jup} would not be detectable. Also, there is an inverse trend for massive satellites, since the incoming flux of the latter for objects with $m_s \sim M_P$ can reach the flux of the planet itself. In these cases, the two fluxes are very much alike and the modulation is not detectable. However, we note that this trend is present only for the very upper part of the mass range tested since the flux rapidly decreases with the mass. We also note that the already unfavorable limit of 20 % would increase further for non-AO observations, making the transit technique somewhat unattractive for the hunting of satellites around DI companions. This is also showcased by the very low probability ($p_i < 2\%$, see Table A1 and A2) of detecting a satellite in the sample of 38 substellar objects considered, as obtained in Section 4.

A first study of photometric variation was applied to HR8799 b and c (Biller et al. 2021) using SPHERE observations. Taking into account the inclination of the system, $\sim 27°$, the derived sensitivity for the two planets is $11-22\%$ and $> 50\%$, respectively. In the same paper, it is also estimated the signal that would be generated by a population of putative transiting satellites injected around HR8799 b, considering the system as seen edge-on.

Photometric variation of a planet can be associated to variable features in the atmospheres, such as clouds. To disentangle the presence of a satellite from the intrinsic mutations of a cloudy atmosphere we could perform multiple observations of the planet at different wavelengths. In fact, if a satellite exhibits, a diminishing in the flux (or a modulation of the latter) it is expected to be almost achromatic and periodic whereas clouds should appear only at certain wavelengths and variable due to their heterogeneous distribution.

[1] This mass-radius relation was derived for systems of different ages. For the very young Jovian planets that we are considering we should expect a larger radius since gravitational contraction is still ongoing.

Photometric observations of isolated planetary mass objects (Limbach et al. 2021) would represent a useful pathway to understand their intrinsic variability and to demonstrate the presence of satellites around these objects. The comparison of the frequency of exomoons around isolated planetary-mass objects with those around planetary companions orbiting stars would also be highly interesting for our understanding of their formation mechanisms.

Even if the orbital separation is not straightforwardly included in the calculation of a transit, the cadence with which the object passes in front of the planet is fundamental to confirming the presence of the former. Continuous or quasi-continuous long-term variability monitoring of directly-imaged planets appears prohibitive in terms of observing time requirements (considering the high-quality AO and then large aperture size needed). Thus, satellites with a short period ($\leq$ 10 days) are more likely to be revealed, limiting in turn the range of detectable satellites around β Pic b.

Another interesting parameter from an observational point of view is the duration of the transit itself given by (Seager & Mallen-Ornelas 2002)

$$T_{tr} = \sqrt{\frac{4a_s^3}{G(m_s + M_P)}} \sin^{-1}\left(\frac{\sqrt{(R_P + R_s)^2 - (bR_P)^2}}{a_s}\right), \quad (5)$$

where b is the impact parameter, i.e. the distance from the center of the planet at which the satellite transits. In Figure 4 an additional plot regarding the transit technique is shown, with the duration of the transit in place of the dimming in the flux (in this case we considered only satellites transiting through the center of the planet, $b = 0$). Considering an instrument from the ground, such as SPHERE, we set an upper limit to the observable time of the transit between 2 and 4 hours. Above this value, variable weather conditions and the increasing distance from meridian passage may strongly influence the observations and the speckles subtraction performed during post-processing (e.g. ADI, PCA). With this further constraint, the zoo of detectable satellites strongly decreases. One possible way to detect satellites with long lasting transits could be to observe the target in different nights with shorter sequences. However, in this case, the photometric precision of the instrument might not be negligible (e.g. the rms scatter of contrast from multi-epoch observations of reference systems with SPHERE was estimated to be typically 0.05-0.08 mag in H band, Langlois et al. 2021a).

The inclination of the planet-satellite system is a crucial parameter to take into account when considering transit observations. As mentioned before, for this test case we considered satellites being coplanar with the orbital plane of the planet. This likely includes objects generated within the circumplanetary disk (regular satellites, Mosqueira & Estrada 2003a,b; Sasaki et al. 2010). The irregular satellites (Nesvorný et al. 2003; Jewitt & Haghighipour 2007; Holt et al. 2018), which are usually the outcome of capture from the surrounding environment, are expected to orbit on inclined orbits. Since, to have a transit, the geometrical condition $cosi_s \leq (R_P + R_s)/a_s$ must be respected, irregular satellites with high values of i_s will pass in front of the parent planet with less probability.

Similar arguments apply to systems which are seen further from edge-on. HR8799 planets, for example, are inclined at $\sim 40°$ with respect to the line of sight (Booth et al. 2016) and any regular satellite would be impossible to detect. Let us consider, for example, the outermost planet, HR8799 b, which has a mass of 6.8 M_{Jup} (Lazzoni, C. et al. 2020a) and thus a radius $R_P = 1.13 R_{Jup}$. If we assume that regular satellites were formed from the circumplanetary disk, we can consider terrestrial-like objects to orbit around HR8799 b. A 1 $M_\oplus$ should orbit at a maximum distance of 7×10^{-4} au to transit in front

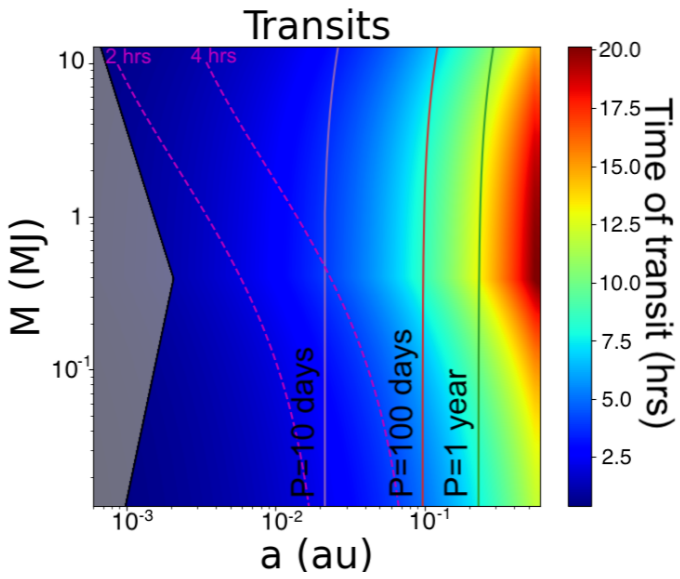

Figure 4. Duration of transits of a population of satellites injected around β Pic b. The orbital periods are represented with purple (10 days), red (100 days) and green (1 year) curves and the Roche limits for tidal disruption is shown in black. The pink dashed line represents the upper limits to the observable time of the transit. The shaded grey area corresponds to the tidal disruption region.

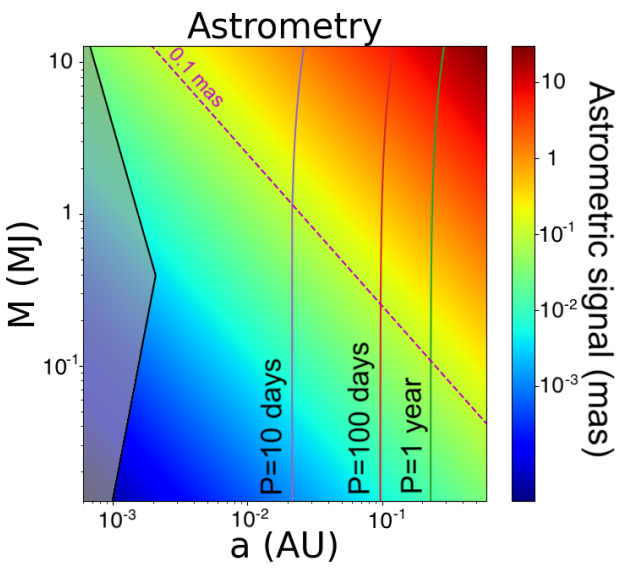

Figure 5. Astrometric signals related to a population of satellites generated around β Pic b. The orbital periods are represented with purple (10 days), red (100 days), green (1 year) and orange (10 years) curves and the Roche limits for tidal disruption is shown in black. The pink dashed line represents the detection limits achievable with GRAVITY. The shaded grey area corresponds to the tidal disruption region.

of the planet, which is at the very limit of disruption due to tidal forces (6.9×10^{-4} au).

It is worth mentioning, however, that the inclination could also have a positive impact on the detectability of a putative satellite since it could significantly decrease the time of the transit, as shown in Equation (5).

3.4 Astrometry

The deviation of the orbit of the planet in the transverse direction due to the presence of the satellite was calculated using

$$\theta = \frac{m_s}{M_P}\frac{a_s}{d} arcsec \quad (6)$$

where d is the distance of the system expressed in parsec. The astrometric measure we consider here is the relative position of the planet with respect to the star; the presence of the satellite is deduced from the residuals of the planet motion with respect to a simple Keplerian orbit around the star. If the planet orbit is much longer than the satellite one, then detection of the wobble due to the satellite does not require to follow the full planet orbit, but only the full satellite orbit. For this reason we set an upper limit of 20 yr to the period of orbits detectable through astrometric signal.

In principle, we cannot tell from this data if the wobbling is due to a satellite around the planet or an additional planet around the star; however, absolute astrometry from Gaia may solve this ambiguity in the near future. Thanks to very precise astrometric measurements performed by instruments such as SPHERE, we are able to detect deviations down to 1 mas (Maire et al. 2021). Even smaller deviations (potentially down to 100 μas, pink dashed line in Fig. 5; see e.g. Lacour et al. (2021)) are achievable with instruments such as GRAVITY/VLTI (Gravity Collaboration et al. 2017) for bright targets ($m_K \sim 10$ mag)[2]. Thus, for β Pic b, the smallest satellite that we should be able to detect if placed at the Hill radius of the planet could have a mass of ~ 0.02 M $_{\rm Jup}$. If we get closer to the planet, the mass of detectable objects significantly increases.

When we consider this technique we have, nevertheless, to take into account other factors. First of all, the better we know the orbit of the planet and the better we can appreciate small deviations from its path. This is, for example, the case of β Pic b that has been observed for more than a decade and, given its relatively small semi-major axis and moderately short orbital period, all the orbital parameters are well constrained. Instead, for most of the planets and brown dwarfs detected with the direct imaging technique only a small portion of the trajectory is known and a family of orbits is considered as possible solutions (Blunt et al. 2017; Maire et al. 2019). In these cases, satellites become detectable only if the astrometric signals generated are not comparable in terms of amplitude and frequency with the motion of the planet around the star. Also, astrometric variations in terms of relative separation between the star and the planet can be due to the presence of further planetary companions around the star. The β Pic system, in this sense, is a very instructive test-bench since it hosts a further planet. β Pic c (Lagrange et al. 2019a) was detected via RV technique so that we can marginally break this degeneracy and isolate its contribution to the relative motion of β Pic b. Assuming, for β Pic c a separation of 2.7 au and a mass of 7.8 M$_{\rm Jup}$ (Lagrange et al. 2019a), the astrometric signal produced by the planet on the parent star is of 0.59 mas. Considering a revolution period for the planet of 3.4 yrs, we can then compare this astrometric signal with the same one, in terms of amplitude and orbital period, that could

[2] Since we are interested here to the relative motion of the planet with respect the star, limiting magnitude of the target we have to consider here is that of the star

be produced by a hypothetical satellite around β Pic b. As shown in Figure 5, a satellite of ~ 0.3 M_{Jup} on a 0.5 au orbit with a period of 3.4 yrs would produce on the b planet a similar astrometric signal as the inner detected planet. Thanks to the detection of β Pic c via radial velocities, we can discard the presence of this kind of satellites. This is only an example of the kind of ambiguity that may arise while considering only the variation in relative separation between the central star and the planet.

Therefore, it stands clear that the association of astrometric variations to the orbit of the planet and the presence of putative satellites around the latter becomes feasible not only when the orbital parameters of the planet are well constrained but also when the system is investigated with other techniques. In fact, the detection/non detection of further planets closer to the star via RV and transits and the absolute astrometry of the star given by GAIA (Gaia Collaboration et al. 2016, 2018) are necessary tools to determine the relative astrometry of the planet and to infer the presence of any satellites bound to it.

4 PROBABILITY OF PLANET DETECTIONS USING THE DIFFERENT METHODS

In this Section we explore the chances of detecting satellites to directly imaged brown dwarfs and planets, in the range of separation from the star between 0.1 and 5 arcsec, that roughly corresponds to semi-major axis in the range from a few to a few hundreds of au.

Hereinafter we will make a first exploration of this field, considering the feasibility of programs that aim to detect satellites around the directly imaged planets using various observation techniques. To this purpose we will first construct a sample of known exoplanets and then consider two different parametric satellite populations around them. For each technique, we will make a first order of magnitude estimate of the detection probability for each of the two satellite populations. We notice that the assumptions we make (e.g. circular orbits; satellites observed in quadrature) are very rough and simplified so that they should be revised for an appropriate interpretation of any specific survey devoted to satellite detection, and that the predictions on the detection probability we give should only be considered as order of magnitude estimates.

4.1 Exoplanet sample

Table 1 contains the main parameters for the sample of exoplanets and brown dwarfs considered throughout our discussion, along with the references from which they were obtained. While quite large, the sample does not have the aim to be complete, but rather to be representative of those systems known at present for which we may reasonably expect satellite detection. We considered 37 planets in 32 systems. We only considered objects with separation in the range between 100 and 5500 mas, because objects at shorter separation are very difficult to observe with the accuracy required to detect satellites with the techniques described in this paper. Moreover, planets and brown dwarfs at such separations have uncertain formation origins and the detection of any satellite around them could give insightful hints on their history. The parameters reported are only those that are used in our probability estimates.

The planet K-band magnitude used in this paper are also given in Table 1. Note that they are derived with the formulas considered in this paper - starting from masses and ages - and they are not the observed values.

4.2 Satellite populations

The probability of a satellite to be detected with a certain technique must be joined with the probability that the same satellite formed with suitable properties to be actually observed. To explore a little further these points, we considered in this paper two different populations of satellites. For simplicity, we will assume that their properties are defined by parametric distributions. Given that we know very little about satellites of exoplanets, we considered two very different populations. Following the approach described in Vigan et al. (2021), we assumed that these two populations are drawn from parametric distributions as a function of the mass ratio q_s between the components (where $q_s \leq 1$) and on the orbital semimajor axis a. In addition, we considered a random on-sky distribution of the satellite orbit inclination i, that is, we will ignore what we know about the planet orbit inclination and the chances that the satellite orbit is coplanar with the planet orbit. The reason for this choice is that for the vast majority of the exoplanets discovered through direct imaging the orbital inclination is very poorly constrained. A significant exception is β Pic b (Lagrange et al. 2019b), that is our archetype.

(i) In analogy with the approach of Vigan et al. (2021), for the first case, we are inspired by typical populations of exoplanets that are thought to form mostly by core accretion; we will then call this population *planet-like*. For the orbital distribution of gas giant planets, we assume a Gaussian distribution in $\log a$, a being the semi-major axis, with fixed mean and σ. These properties likely depend on the host star mass and based on results to date, we adopt a log-normal distribution with a $\sigma = 0.52$, as used for M stars (Meyer et al. 2018; Fernandes et al. 2019). For the mean value, instead, we used the expression $a = \log_{10}(0.45 * (M_P/30.0)^{0.77})$, where M_P is the mass of the planet expressed in Jupiter masses. This formula was obtained by assuming that the peak of the satellite formation is close to the ice-line around very young planets. This position was then derived by fitting the isochrones at 1 Myr from Baraffe et al. (2003). Since this population is thought to form through core accretion within a circumplanetary disk, the relevant typical value for a is fixed here in relation to the snow-line. This depends on the planet luminosity which, in turn, depends on the mass and age - at the epoch of formation of the satellite (that is not the current age of the system). For reference we considered an age of 1 Myr and derived the luminosity using the DUSTY-AMES isochrones by Allard et al. (2001). As to the planet mass function, we assume a power-law where the frequency f depends on the ratio of the satellite to the planet mass, $q_s = M_s/M_p$, that is $f \propto q_s^{\beta}$, with $\beta = -1.31$ (Cumming et al. 2008; Wagner et al. 2019). To estimate the probability of finding such satellites, we may assume that 10% of the planets have a satellite with $q_s > 0.0003$, similar to the frequency of giant planets (Cumming et al. 2008). To place these values in a context, the Titan/Saturn system has a mass ratio equal to $q_s = 0.00024$ and Titan is approximately at 60% of the peak of the separation distribution we assumed. Hence, Titan would be quite a typical satellite extracted from such a distribution.

(ii) The second population of satellites we considered is under the assumption that planet-satellite systems are analogues to binary systems. We call this population *binary-like*. Given the typical range of separations from the parent planet/BD, this population might have formed through fragmentation/instability of the disk around it - likely very early in the formation phase of this system -, fragmentation of the cloud/filament from which the star formed, or by captures (Ochiai et al. 2014). For similarity with the stellar binary case we assumed a log-normal semi-major axis distribution of binary companions, as measured for stellar masses (e.g. Raghavan et al. 2010 for FGK

Table 1. Planets and brown dwarfs parameters

Planet Name	Age Myr	Parallax mas	K_* mag	K_P mag	Sep mas	a au	M_* $M_\odot$	M_P M_J	Ref
1RXS J160929.1-210524 b	10.0	7.16	8.916	16.9	2,215.0	309.4	0.85	8.0	Lafrenière et al. (2008, 2010)
2M1207 b	8.0	19.08	11.945	15.6	878.0	42.0	0.03	5.0	Chauvin et al. (2004b)
51 Eri b	24.0	33.58	4.537	>21	434.0	11.2	1.75	3.6	De Rosa et al. (2020b)
AB Pic b	45.0	19.95	6.981	15.1	5,400.0	270.6	0.86	14.0	Langlois et al. (2021b)
beta Pic b	16.0	51.44	3.480	14.9	510.8	8.9	1.64	12.8	Desidera et al. (2021); Lagrange et al. (2019b)
CT Cha b	1.4	5.21	8.661	14.8	2,680.0	514.0	0.80	15.0	Sheehan et al. (2019)
DH Tau B	1.4	7.39	8.824	14.7	2,350.0	318.1	0.10	10.6	Lazzoni, C. et al. (2018); Sheehan et al. (2019)
eta Tel B	24.0	21.11	5.010	13.2	4,210.0	199.4	2.18	47.0	Langlois et al. (2021b)
GJ504 b	4000.0	56.86	4.033	>21	2,490.0	43.8	1.18	23.0	Bonnefoy et al. (2018)
GQ Lup b	3.5	6.59	7.096	13.5	712.0	117.0	1.03	30.0	Stolker et al. (2021)
HD1160 c	50.0	7.94	7.040	14.2	773.0	97.3	2.00	66.0	Mesa et al. (2020)
HD4747 B	2300.0	51.95	5.305	13.6	590.0	11.4	0.86	70.0	Peretti et al. (2019)
HD19467 B	8000.0	31.22	5.401	14.2	1,631.0	44.1	0.95	74.0	Maire et al. (2020b)
HD72946 B	1600.0	38.65	5.467	13.5	235.0	6.5	0.99	72.4	Maire et al. (2020a)
HD95086 b	12.0	11.57	6.789	> 21	630.1	58.0	1.60	4.5	Desgrange et al. (2022)
HR2562 B	750.0	29.41	5.020	17.4	640.0	21.8	1.37	29.0	Sutlieff et al. (2021)
HR3549 B	125.0	10.49	6.044	16.8	850.0	81.1	2.00	48.0	Mesa et al. (2016)
HR8799 b	42.0	24.22	5.240	20.6	1,720.6	72.2	1.52	5.8	Zurlo et al. 2022, accepted
HR8799 c	42.0	24.22	5.240	18.2	955.1	41.6	1.52	7.6	Zurlo et al. 2022, accepted
HR8799 d	42.0	24.22	5.240	16.9	689.8	26.9	1.52	9.2	Zurlo et al. 2022, accepted
HR8799 e	42.0	24.22	5.240	18.2	397.2	16.3	1.52	7.6	Zurlo et al. 2022, accepted
HIP64892 B	16.0	7.99	6.832	16.3	1,270.5	159.1	2.35	33.0	Cheetham et al. (2018)
HIP65426 b	14.0	9.16	6.771	> 21	824.0	115.0	1.96	8.0	Chauvin et al. (2017)
HIP74865 B	15.0	8.10	7.808	15.7	201.0	24.8	1.72	46.0	Hinkley et al. (2015)
HIP78530 B	11.0	7.28	6.903	18.4	4,180.0	573.8	2.75	20.0	Langlois et al. (2021b)
HIP79098 B	10.0	6.83	5.707	14.7	2,359.0	345.2	4.00	20.0	Janson et al. (2019)
HIP107412 B	700.0	24.51	5.593	17.6	252.2	12.8	1.32	25.0	Romero et al. (2021)
k And b	47.0	20.00	4.320	13.9	875.6	103.6	2.70	20.0	Carson et al. (2013)
PDS 70 b	5.4	8.82	8.542	15.2	173.5	20.1	0.98	7.9	Wang et al. (2021)
PDS 70 c	5.4	8.82	8.542	15.2	213.2	33.2	0.98	7.8	Wang et al. (2021)
PZ Tel B	24.0	21.22	6.366	13.0	558.0	70.9	0.90	52.0	Maire et al. (2016a)
TYC 7084-794-1 B	140.0	44.63	7.046	15.3	2,990.0	67.0	0.50	32.0	Langlois et al. (2021b)
TYC 8047-232-1 B	42.0	11.59	8.405	16.4	3,210.0	277.0	0.82	13.8	Langlois et al. (2021b)
TYC 8998-760-1 b	17.0	10.57	8.392	18.2	1,712.5	162.0	1.00	14.0	Bohn et al. (2020)
TYC 8998-760-1 c	17.0	10.57	8.392	> 21	3,373.0	320.0	1.00	6.0	Bohn et al. (2020)
TYC 8984-2245-1 b	13.9	9.09	8.358	> 21	1,050.0	115.0	1.10	6.3	Bohn et al. (2021)
GSC 6214-210 B	10.0	9.19	9.152	14.8	2,205.1	240.0	0.90	14.0	Pearce et al. (2019)

stars and Winters et al. 2019 for M dwarfs) with mean $\log a = 1.30$ and $\sigma = 1.16$. For this population, we assume a companion mass ratio distribution, which is roughly flat with the mass ratio (power-law slope of 0.25; Reggiani & Meyer 2013) with a minimum mass ratio of $q_s = 0.01$. When estimating the probability of finding similar satellites, we may assume that 20% of the planets have such a satellite that is not far from the typical fraction of binaries among small mass stars (Moe & Di Stefano 2017). As a reference, the BD binary companions to ϵ Ind have a mass ratio $q \sim 0.6$ and are at a projected separation of 26 au from each other (McCaughrean et al. 2004) at about 1500 au from the star, that is around 0.05 times the Hill radius. So they may be considered representative of this population.

In both cases we assume that the satellites should lie within the allowed range of semimajor axis between the Roche limit and 0.5 times the Hill radius.

4.3 Detection limits

4.3.1 Direct Imaging

We assume that the limiting satellite star contrast depends on three factors: (i) the noise associated to sky background, c_s (this is a term that only depends on the satellite apparent magnitude); (ii) the noise associated to primary background, c_*(depends on the K magnitude of the primary and on star-planet separation, neglecting the difference between planet and satellite separation); and (iii) the noise associated to planet background, c_p (depends on the K magnitude of the planet and on planet-satellite separation). The following calculations are obtained assuming good-quality observations of 1 hr taken from a 8-meter size telescope during meridian passage.

We may write the limiting contrast as

$$c_{\rm lim} = -2.5 \log \sqrt{10^{-0.8c_{\rm s}} + 10^{-0.8c_*} + 10^{-0.8c_{\rm p}}} \quad (7)$$

where the contrasts are in magnitudes.

The sky background limiting contrast in the K-band is

$$c_s = 19.6 + const \quad (8)$$

The sky background is from Cuby et al. (2000) but refers to a sky area equal to $\pi(0.5\lambda/D)^2$, where λ is the observing wavelength and D is the telescope diameter. The constant term should account for the fact that here we are interested to the noise associated to the sky background, a quantity that depends on the square root of the number of sky photons detected. In practice, we find $const = 4.2$ mag.

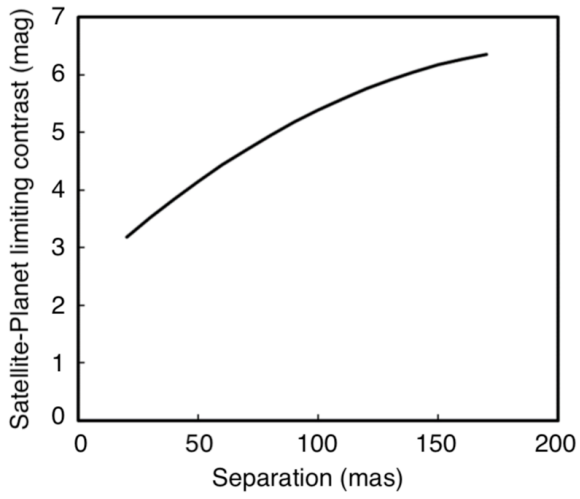

Figure 6. Assumed planet-satellite limiting contrast as a function of separation

For what concerns the stellar background, we may use an interpolatory form described in Langlois et al. (2021b), which describes a median observation with SPHERE. Limiting contrast in good conditions might approximately be better by 0.75 mag. If K_* is the star K-band magnitude and d is the star-planet separation in mas, assuming typical values for the number of Detector Integration Time (DIT), $n_{\rm DIT} = 48$, for the total exposure time $t_{\rm exp} = 72s \times n_{\rm DIT}$, and for the inclination of the system, $\alpha = 60°$, we can define the following parameters

$$r = 20.7 - K_* + 1.25 \log t_{\rm exp}/3600$$
$$s = 20.7 + 1.25 \log n_{\rm DIT}/4.6 - K_* + 1.25 \log 10 t_{\rm exp}/3600$$
$$p = 17.07 + 3.0(500/d) \log \alpha/60 + 8.75 \log d/500$$
$$q = -0.5K_* + 18.05 + 1.25 \log t_{\rm exp}/3600 + 4.375 \log d/500$$
$$c_* = -2.5 \log \sqrt{10^{-0.8p} + 10^{-0.8q} + 10^{-0.8r} + 10^{-0.8s}}$$

For the planet background, we interpolated a formula through the planet-satellite limiting contrast curve derived in Lazzoni, C. et al. (2020b) for DH Tau. If x is the satellite-planet separation in mas and ΔK_p is the star planet- contrast in the K-band, then:

$$c_p = \Delta K_p + (-9.132 * 10^{-5} * x^2 + 3.85 * 10^{-2} * x + 2.452)$$

This formula is valid for separation < 220 mas. At larger separation the contrast due to the planet is negligible with respect to that due to the sky. Figure 6 shows the limiting contrast for satellite detection due to the planet background as a function of planet-satellite separation provided by this formula. Note that this sums in quadrature with other sources of background as given by eq. (7), so that the actual limit may be brighter depending on the particular planet we consider. The estimation for the contrast given in this Section are to be considered only as an order of magnitude more than a precise result. For example, for the β Pic system, from Figure 1 we obtain that the minimum detectable mass is $\sim$ 11.1 $M_{\rm Jup}$, which correspond to $q = 0.87$. From Table A1, we retrieved a minimum value for the mass ratio of 0.59. The discrepancy between the two results is mostly given by the different procedures followed when retrieving the K_P magnitudes for β Pic b: from observations in Section 3 and from the mass using interpolated equations in this Section.

4.3.2 Radial velocities

Considering the discussion presented in Section 3.2, we assumed that the limiting detectable amplitude of a radial velocity signal by a satellite is $0.1 \times 10^{0.2(K_P - 13.5)}$ km/s. This is true for objects with magnitudes close to $K_p \lesssim 15$ (such as β Pic b), whereas for less bright planets we are mostly limited by background noise and the detection probability decreases much more quickly. Thus, the estimates given in Tables A1 and A2 are slightly optimistic when considering the dimmest substellar objects. We also assumed that only satellites with periods shorter than 20 yr can be discovered using radial velocities.

We note that when considering the whole sample considered in Table 1, the gain using best performing AO but lower transmission of HiRISE with respect to MACAO should be considered object-by-object.

4.3.3 Transits

We assumed that transits may be detected if the transit signal corresponds to at least a 20% dimming of the flux of the planet/BD, as mentioned in Section 3.3. We also assumed that only satellites with periods shorter than 0.1 yr can be discovered using transits.

4.3.4 Astrometry

Considering the discussion presented in Section 3.4, we assumed that the limiting detectable amplitude of an astrometric signal by a satellite is 0.3 mas. This corresponds to a 3 σ detection within a sequence of observations done with Gravity. We also assumed that only satellites with periods shorter than 20 yr can be discovered using astrometry.

4.4 Results

Tables A1 and A2 give the detection probability and detected satellite parameters for the binary-like and planet-like satellite populations, respectively. As mentioned above, we should multiply these probabilities for the expected frequencies of satellites around planets.

If we do a survey of these 38 planets and brown dwarfs found by direct imaging, the probability of finding at least one satellite depends on the technique used and on the real satellite population. In Table 2 we give the probability of detecting at least one satellite around one planet/BD by observing the whole sample. The probability of the detection of at least one satellite by observation of the whole sample of 38 planets/BDs, $P_{\rm tot}$, is different from the probability p_i of detecting a satellite around each planet in the sample (reported in Tables A1 and A2). The relation between these two probabilities is:

$$P_{\rm tot} = 1 - \prod 1 - p_i \quad (9)$$

In all cases, the probabilities do not only depend on the satellite detectability, but also on the actual frequency of satellites in the population considered. We then give two values for $P_{\rm tot}$, for a frequency f=1 (all planets have one satellite belonging to that particular population) and more realistic values obtained considering a lower frequency of f=0.14 for the binary-like population and of f=0.3 for the *planet-like* satellite population. Though the latter two frequencies were chosen rather arbitrarily to give order of magnitude estimates, they were inspired by the the frequency of companions to low-mass stars (Fischer & Marcy 1992; Delfosse et al. 2004; Janson et al. 2012) and the frequency of giant planets around Solar-type stars (see e.g. Table 1 of Rameau et al. 2013) In general, the probability of finding

at least one satellite is reasonably high if satellites distribute according to the binary distribution, that is, if planets and satellites form like binaries by cloud or disk fragmentation or by capture. It is low, instead, if satellites around planets are distributed as planets around stars, that is if they are formed within a core accretion scenario. Even limiting to the first class of objects, the satellites that can be found around direct imaging planets depends on the technique used (see Table 3). Direct imaging is only sensitive to satellites at rather large separations; astrometry and radial velocities probes regions at intermediate separations; while transits can only reveal satellites very close to the planets. In addition, imaging may only reveal satellites with large mass ratio, and hence only those formed in a *binary-like* scenario.

When considering campaigns devoted to searching for satellites, we found that the DI technique is by far the least costly in terms of telescope time. In fact, indirect techniques require tens of observations spread over long time intervals. The observing time required to obtain the temporal series required by RV and transit methods for all the planets in the sample is huge (about 2000-4000 hr on an 8 m telescope). Much less observing time ($\sim$ 100 hr) is required by direct imaging, while the request for astrometry is intermediate between the two values, but still considerable (about 1000-2000 hr). On the other hand, in principle a single visit is enough to detect a satellite by DI, though of course a few more are likely required for confirmation and characterization. It can then be useful to consider the probability of detection of at least one satellite for a given observing time (say 100 hr). Here, we only consider the detection of binary-like satellites, because the probability of detecting planet-like satellites within this observing time is always very small. Since for direct imaging we may observe the whole sample, $P_{\rm tot}$ is still that given in Table 2, that is 97.2% if f=1 and 36% if f=0.14. Within 100 hr we may obtain adequate time series for RV and transits only for a couple of planets; selecting best candidates, using RVs we have $P_{\rm tot}$ = 42% if f=1 and 6% if f=0.14; for transits the probabilities are $P_{\rm tot}$ = 3% if f=1 and less than 1% if f=0.14. For astrometry we might observe four targets, yielding $P_{\rm tot}$ = 64% if f=1 and 12% if f=0.14. This clarifies that DI is the most efficient technique, in terms of observing time, for binary-like planets, with astrometry and radial velocities also being interesting possible alternatives.

From this point of view, notably Lazzoni, C. et al. (2020b) found a candidate satellite to DH Tau B in their DI survey with a mass ratio $q \sim 0.1$ at $\sim$ 10 au from the companion. The parameters for this object is similar to those considered here for the *binary-like* population. This is particularly intriguing because this is indeed the target with the highest probability of detection of a satellite through DI among those considered in this paper. While this satellite still needs a final confirmation, it shows the possible expectations for a search of satellites through DI.

We notice that the prospects for a satellite search through DI are even better when using ELT because of the much higher spatial resolution that allows observation of satellites at much closer separations than is possible with 8-m telescopes. As an example, we may estimate that simply because of the higher space resolution, the probability of finding a binary-like satellite around GQ Lup b (if it is there) increases from 17 to 30% when migrating from VLT to ELT.

5 SUMMARY

In this paper we presented an analysis of the detectability, with different techniques, of satellites around directly imaged planets and brown dwarfs. The term satellite is still vague and could include *planet-like* companions, similar to the moons of the Solar system, or *binary-like* companions, with mass ratio with respect to the planet close to 1.

Table 2. Probability of detecting at least one satellite and expected number of detected satellites extracted from different distributions with different techniques; f is the frequency of giant satellites per planet

Technique	binary-like		N_{det}	planet-like		N_{det}
	f=1.0	f=0.14	f=1.0	f=1.0	f=0.3	f=1.0
Astrometry	0.999	0.58	6.1	0.08	0.024	0.08
Imaging	0.965	0.35	3.2	0.00	0.000	0.00
RV	0.996	0.52	5.1	0.08	0.025	0.08
Transits	0.433	0.08	0.6	0.06	0.019	0.06

Table 3. Median orbital semimajor axis, a, in au and mass ratio $q = m_s/M_P$ expected for detected satellites extracted from different distributions with different techniques

Technique	Median(a)	Median(q)	Median(a)	Median(q)
	binary-like		planet-like	
Astrometry	0.60	0.52	0.66	0.066
Imaging	2.68	0.62		
RV	0.57	0.52	0.15	0.050
Transits	0.030	0.45	0.034	0.012

Directly imaged exoplanets and brown dwarfs look quite promising for the search of satellites thanks to their mass and wide separation from the host star. These conditions could in principle permit the existence of a zoo of satellites with a wide range of masses and separations from the planet. Moreover, the formation history of DI substellar companions is not yet well established and could be inferred by the properties of any putative satellite.

We showed our complete results for a test system, β Pic b, plotting the signals that each satellite, under the simplistic assumptions of circular orbits and most favorable inclination angles, could generate if the planet were observed with different techniques. We then generated two populations of satellites, *planet-like* and *binary-like* respectively, on circular orbits and inclinations distributed according to *sini*, around a sample of 38 DI exoplanets and brown dwarfs and we analyzed their detectability with different techniques (direct imaging, RV, transits and astrometry). From this preliminary analysis it emerged that *planet-like* satellites around substellar companions have very low chances of being detected at present times with any technique (highest probability values of $\sim$ 0.01 for RV and Astrometry). On the other hand, a significant fraction of *binary-like* satellites, if present, would be revealed. For this second category of satellites, given the similar detection probabilities for the four techniques analyzed, direct imaging is the most suitable tool for this kind of survey since it requires less observations, compared to any indirect methods, to confirm a candidate.

We also note that new techniques are being studied for the characterization of exoplanets/BD and the search of satellites, such as spectroastrometry and molecular mapping. Spectroastrometry consists of measuring very accurately the position of the photocenter emitted from an unresolved system companion+satellite for each wavelength of a spectrum. This technique could be particularly efficient using instruments such as SPIFFIER+ERIS (George et al. 2016; Amara & Quanz 2012; Kenworthy et al. 2018) and, in the future, JWST/NIRSpec (Birkmann et al. 2016), SPHERE+ (Boccaletti et al. 2020), or HARMONI (the IFU of the ELT) (Thatte et al.

2021). Molecular mapping (Sparks & Ford 2002; Konopacky et al. 2013), instead, consists in the coupling of AO instruments with high-resolution spectrograph to disentangle the contribution of putative satellites from the central planet/BD. Instruments such as CRIRES+ (Follert et al. 2014) and ERIS+SPIFFIER (Kenworthy et al. 2018) will be the first to push to the limits of the detection capabilities of this technique, though first analyses were already attempted with SINFONI (Hoeijmakers et al. 2018).

To conclude, all the techniques mentioned will give outstanding results in the search for satellites thanks to the arrival of new instruments and facilities operating both from ground and space, in the near future.

ACKNOWLEDGEMENTS

This work has been supported by the PRIN-INAF 2019 "Planetary systems at young ages (PLATEA). A.Z. acknowledges support from the FONDECYT Iniciación en investigación project number 11190837. We also acknowledge financial support from the ASI-INAF agreement n.2018-16-HH.0. For the purpose of open access, the authors have applied a Creative Commons Attribution (CC BY) licence to any Author Accepted Manuscript version arising from this submission.

DATA AVAILABILITY

Data used in this paper is available from the authors upon reasonable request.

REFERENCES

Agnor C. B., Hamilton D. P., 2006, Nature, 441, 192
Allard F., Hauschildt P. H., Alexander D. R., Tamanai A., Schweitzer A., 2001, ApJ, 556, 357
Amara A., Quanz S. P., 2012, MNRAS, 427, 948
Baraffe I., Chabrier G., Barman T. S., Allard F., Hauschildt P. H., 2003, A&A, 402, 701
Bashi D., Helled R., Zucker S., Mordasini C., 2017, A&A, 604, A83
Benz W., Slattery W. L., Cameron A. G. W., 1986, Icarus, 66, 515
Biller B. A., et al., 2021, arXiv e-prints, p. arXiv:2101.08514
Birkmann S. M., et al., 2016, in MacEwen H. A., Fazio G. G., Lystrup M., Batalha N., Siegler N., Tong E. C., eds, Society of Photo-Optical Instrumentation Engineers (SPIE) Conference Series Vol. 9904, Space Telescopes and Instrumentation 2016: Optical, Infrared, and Millimeter Wave. p. 99040B, doi:10.1117/12.2231837
Blunt S., et al., 2017, AJ, 153, 229
Boccaletti A., et al., 2020, arXiv e-prints, p. arXiv:2003.05714
Bohn A. J., et al., 2020, ApJ, 898, L16
Bohn A. J., et al., 2021, A&A, 648, A73
Bonnefoy M., et al., 2018, A&A, 618, A63
Booth M., et al., 2016, MNRAS
Boss A. P., 1997, Science, 276, 1836
Brandl B. R., et al., 2010, in McLean I. S., Ramsay S. K., Takami H., eds, Society of Photo-Optical Instrumentation Engineers (SPIE) Conference Series Vol. 7735, Ground-based and Airborne Instrumentation for Astronomy III. p. 77352G, doi:10.1117/12.857346
Cameron A. G. W., 1978, Moon and Planets, 18, 5
Cameron A. G. W., Ward W. R., 1976, in Lunar and Planetary Science Conference. p. 120
Canup R. M., 2004, ARA&A, 42, 441
Canup R. M., 2005, Science, 307, 546
Canup R. M., Ward W. R., 2002, AJ, 124, 3404
Canup R. M., Ward W. R., 2006, Nature, 441, 834
Carson J., et al., 2013, ApJ, 763, L32
Chauvin G., Lagrange A. M., Dumas C., Zuckerman B., Mouillet D., Song I., Beuzit J. L., Lowrance P., 2004a, A&A, 425, L29
Chauvin G., Lagrange A. M., Dumas C., Zuckerman B., Mouillet D., Song I., Beuzit J. L., Lowrance P., 2004b, A&A, 425, L29
Chauvin G., et al., 2017, A&A, 605, L9
Chauvin G., et al., 2018, A&A, 617, A76
Cheetham A., et al., 2018, A&A, 615, A160
Cheetham A. C., et al., 2019, A&A, 622, A80
Climent J. B., Berger J. P., Guirado J. C., Marcaide J. M., Martí-Vidal I., Mérand A., Tognelli E., Wittkowski M., 2019, arXiv e-prints, p. arXiv:1911.04736
Cuby J. G., Lidman C., Moutou C., 2000, The Messenger, 101, 2
Ćuk M., Burns J. A., 2004, Icarus, 167, 369
Cumming A., Butler R. P., Marcy G. W., Vogt S. S., Wright J. T., Fischer D. A., 2008, PASP, 120, 531
Danielski C., Baudino J.-L., Lagage P.-O., Boccaletti A., Gastaud R., Coulais A., Bézard B., 2018, AJ, 156, 276
De Rosa R. J., et al., 2015, ApJ, 814, L3
De Rosa R. J., et al., 2020a, Journal of Astronomical Telescopes, Instruments, and Systems, 6, 015006
De Rosa R. J., et al., 2020b, AJ, 159, 1
Delfosse X., et al., 2004, in Hilditch R. W., Hensberge H., Pavlovski K., eds, Astronomical Society of the Pacific Conference Series Vol. 318, Spectroscopically and Spatially Resolving the Components of the Close Binary Stars. pp 166–174
Delorme P., et al., 2017, A&A, 608, A79
Desgrange C., et al., 2022, arXiv e-prints, p. arXiv:2206.00425
Desidera S., et al., 2021, arXiv e-prints, p. arXiv:2103.04366
Domingos R. C., Winter O. C., Yokoyama T., 2006, MNRAS, 373, 1227
Farinato J., et al., 2015, in Adaptive Optics for Extremely Large Telescopes IV (AO4ELT4). p. E69
Femenía B., et al., 2011, MNRAS, 413, 1524
Fernandes R. B., Mulders G. D., Pascucci I., Mordasini C., Emsenhuber A., 2019, ApJ, 874, 81
Figueira P., et al., 2010, A&A, 511, A55
Fischer D. A., Marcy G. W., 1992, ApJ, 396, 178
Follert R., et al., 2014, in Ramsay S. K., McLean I. S., Takami H., eds, Society of Photo-Optical Instrumentation Engineers (SPIE) Conference Series Vol. 9147, Ground-based and Airborne Instrumentation for Astronomy V. p. 914719, doi:10.1117/12.2054197
Fusco T., et al., 2016, in Marchetti E., Close L. M., Véran J.-P., eds, Society of Photo-Optical Instrumentation Engineers (SPIE) Conference Series Vol. 9909, Adaptive Optics Systems V. p. 99090U, doi:10.1117/12.2233319
Gaia Collaboration et al., 2016, A&A, 595, A1
Gaia Collaboration et al., 2018, A&A, 616, A1
George E. M., et al., 2016, in Evans C. J., Simard L., Takami H., eds, Society of Photo-Optical Instrumentation Engineers (SPIE) Conference Series Vol. 9908, Ground-based and Airborne Instrumentation for Astronomy VI. p. 99080G (arXiv:1608.02457), doi:10.1117/12.2231285
Goldreich P., Murray N., Longaretti P. Y., Banfield D., 1989, Science, 245, 500
Goździewski K., Migaszewski C., 2020, ApJ, 902, L40
Gravity Collaboration et al., 2017, A&A, 602, A94
Gravity Collaboration et al., 2019, A&A, 623, L11
Heller R., 2016, A&A, 588, A34
Heller R., Albrecht S., 2014, ApJ, 796, L1
Heller R., Rodenbeck K., Bruno G., 2019, A&A, 624, A95
Hinkley S., et al., 2015, ApJ, 806, L9
Hoeijmakers H. J., Schwarz H., Snellen I. A. G., de Kok R. J., Bonnefoy M., Chauvin G., Lagrange A. M., Girard J. H., 2018, A&A, 617, A144
Holt T. R., Brown A. J., Nesvorný D., Horner J., Carter B., 2018, ApJ, 859, 97
Inderbitzi C., Szulágyi J., Cilibrasi M., Mayer L., 2020, MNRAS, 499, 1023
Janson M., et al., 2012, ApJ, 754, 44
Janson M., et al., 2019, A&A, 626, A99
Jewitt D., Haghighipour N., 2007, ARA&A, 45, 261

Kasper M., et al., 2021, The Messenger, 182, 38
Kenworthy M. A., et al., 2018, in Evans C. J., Simard L., Takami H., eds, Society of Photo-Optical Instrumentation Engineers (SPIE) Conference Series Vol. 10702, Ground-based and Airborne Instrumentation for Astronomy VII. p. 1070246, doi:10.1117/12.2313964
King R. R., McCaughrean M. J., Homeier D., Allard F., Scholz R. D., Lodieu N., 2010, A&A, 510, A99
Kipping D., et al., 2022, Nature Astronomy,
Kirkpatrick J. D., Dahn C. C., Monet D. G., Reid I. N., Gizis J. E., Liebert J., Burgasser A. J., 2001, AJ, 121, 3235
Koch F. E., Hansen B. M. S., 2011, MNRAS, 416, 1274
Konopacky Q. M., Barman T. S., Macintosh B. A., Marois C., 2013, Science, 339, 1398
Konopacky Q. M., et al., 2016, ApJ, 829, L4
Kreidberg L., Luger R., Bedell M., 2019, ApJ, 877, L15
Kuzuhara M., et al., 2013, ApJ, 774, 11
Lacour S., et al., 2021, A&A, 654, L2
Lafrenière D., Jayawardhana R., van Kerkwijk M. H., 2008, ApJ, 689, L153
Lafrenière D., Marois C., Doyon R., Barman T., 2009, ApJ, 694, L148
Lafrenière D., Jayawardhana R., van Kerkwijk M. H., 2010, ApJ, 719, 497
Lagrange A.-M., et al., 2010, Science, 329, 57
Lagrange A. M., et al., 2019a, Nature Astronomy, 3, 1135
Lagrange A. M., et al., 2019b, A&A, 621, L8
Langlois M., et al., 2021a, arXiv e-prints, p. arXiv:2103.03976
Langlois M., et al., 2021b, A&A, 651, A71
Larson R. B., 1985, MNRAS, 214, 379
Lazzoni, C. et al., 2018, A&A, 611, A43
Lazzoni, C. et al., 2020a, A&A, 635, L11
Lazzoni, C. et al., 2020b, A&A, 641, A131
Limbach M. A., Vos J. M., Winn J. N., Heller R., Mason J. C., Schneider A. C., Dai F., 2021, ApJ, 918, L25
Linder E. F., Mordasini C., Mollière P., Marleau G.-D., Malik M., Quanz S. P., Meyer M. R., 2019, A&A, 623, A85
Luhman K. L., Allers K. N., Jaffe D. T., Cushing M. C., Williams K. A., Slesnick C. L., Vacca W. D., 2007, ApJ, 659, 1629
Maire A. L., et al., 2016a, A&A, 587, A56
Maire A.-L., et al., 2016b, in Proc. SPIE. p. 990834 (arXiv:1609.06681), doi:10.1117/12.2233013
Maire A. L., et al., 2019, A&A, 624, A118
Maire A. L., et al., 2020a, A&A, 633, L2
Maire A. L., et al., 2020b, A&A, 639, A47
Maire A. L., et al., 2021, The Messenger, 183, 7
Marleau G.-D., Coleman G. A. L., Leleu A., Mordasini C., 2019, A&A, 624, A20
McCaughrean M. J., Close L. M., Scholz R. D., Lenzen R., Biller B., Brandner W., Hartung M., Lodieu N., 2004, A&A, 413, 1029
McKinnon W. B., 1989, ApJ, 344, L41
Mesa D., et al., 2016, A&A, 593, A119
Mesa D., et al., 2018, A&A, 612, A92
Mesa D., et al., 2020, MNRAS, 495, 4279
Meyer M. R., Amara A., Reggiani M., Quanz S. P., 2018, A&A, 612, L3
Mizuno H., 1980, Progress of Theoretical Physics, 64, 544
Moe M., Di Stefano R., 2017, ApJS, 230, 15
Mosqueira I., Estrada P. R., 2003a, Icarus, 163, 198
Mosqueira I., Estrada P. R., 2003b, Icarus, 163, 232
Mosqueira I., Estrada P., Turrini D., 2010, Space Sci. Rev., 153, 431
Müller A., et al., 2018, A&A, 617, L2
Nesvorný D., Bottke William F. J., Dones L., Levison H. F., 2002, Nature, 417, 720
Nesvorný D., Alvarellos J. L. A., Dones L., Levison H. F., 2003, AJ, 126, 398
Nesvorný D., Vokrouhlický D., Morbidelli A., 2007, AJ, 133, 1962
Ochiai H., Nagasawa M., Ida S., 2014, ApJ, 790, 92
Otten G. P. P. L., et al., 2021, A&A, 646, A150
Paufique J., et al., 2006, arXiv e-prints, pp astro–ph/0608011
Pearce L. A., Kraus A. L., Dupuy T. J., Ireland M. J., Rizzuto A. C., Bowler B. P., Birchall E. K., Wallace A. L., 2019, AJ, 157, 71
Peretti S., et al., 2019, A&A, 631, A107
Podsiadlowski P., Rappaport S., Fregeau J. M., Mardling R. A., 2010, arXiv e-prints, p. arXiv:1007.1418
Potter D., Martín E. L., Cushing M. C., Baudoz P., Brandner W., Guyon O., Neuhäuser R., 2002, ApJ, 567, L133
Raghavan D., et al., 2010, ApJS, 190, 1
Rameau J., et al., 2013, A&A, 553, A60
Raymond S. N., 2015, Hill Radius/Sphere. Springer Berlin Heidelberg, Berlin, Heidelberg, pp 1110–1111, doi:10.1007/978-3-662-44185-5_724, https://doi.org/10.1007/978-3-662-44185-5_724
Reggiani M., Meyer M. R., 2013, A&A, 553, A124
Reufer A., Meier M. M. M., Benz W., Wieler R., 2012, Icarus, 221, 296
Rodenbeck K., Heller R., Hippke M., Gizon L., 2018, A&A, 617, A49
Rodenbeck K., Heller R., Gizon L., 2020, A&A, 638, A43
Romero C., Milli J., Lagrange A. M., van Holstein R. G., Cantalloube F., Marino S., Ray S., 2021, A&A, 651, A34
Rozner M., Grishin E., Perets H. B., 2020, MNRAS, 497, 5264
Ruffio J.-B., et al., 2019, AJ, 158, 200
Sasaki T., Stewart G. R., Ida S., 2010, ApJ, 714, 1052
Schwarz H., Ginski C., de Kok R. J., Snellen I. A. G., Brogi M., Birkby J. L., 2016, A&A, 593, A74
Seager S., Mallen-Ornelas G., 2002, arXiv e-prints, pp astro–ph/0210076
Sheehan P. D., Wu Y.-L., Eisner J. A., Tobin J. J., 2019, ApJ, 874, 136
Snellen I. A. G., Brandl B. R., de Kok R. J., Brogi M., Birkby J., Schwarz H., 2014, Nature, 509, 63
Sparks W. B., Ford H. C., 2002, ApJ, 578, 543
Stolker T., et al., 2021, AJ, 162, 286
Sutlieff B. J., et al., 2021, MNRAS, 506, 3224
Teachey A., Kipping D. M., 2018, Science Advances, 4, eaav1784
Thatte N., et al., 2021, The Messenger, 182, 7
Van Leeuwen F., 2007, A&A, 474, 653
Vanderburg A., Rappaport S. A., Mayo A. W., 2018, AJ, 156, 184
Vigan A., et al., 2018, in Evans C. J., Simard L., Takami H., eds, Society of Photo-Optical Instrumentation Engineers (SPIE) Conference Series Vol. 10702, Ground-based and Airborne Instrumentation for Astronomy VII. p. 1070236 (arXiv:1806.10618), doi:10.1117/12.2313681
Vigan A., et al., 2021, A&A, 651, A72
Vigan A., et al., 2022, arXiv e-prints, p. arXiv:2207.06436
Vokrouhlický D., Nesvorný D., Levison H. F., 2008, AJ, 136, 1463
Wagner K., Apai D., Kratter K. M., 2019, ApJ, 877, 46
Wahhaj Z., et al., 2021, A&A, 648, A26
Wang J. J., et al., 2018, AJ, 156, 192
Wang J. J., et al., 2021, AJ, 161, 148
Winters J. G., et al., 2019, AJ, 157, 216
Woolfson M. M., 1999, MNRAS, 304, 195
Wright J. T., 2018, Radial Velocities as an Exoplanet Discovery Method. p. 4, doi:10.1007/978-3-319-55333-7_4
Xuan J. W., Bryan M. L., Knutson H. A., Bowler B. P., Morley C. V., Benneke B., 2020, AJ, 159, 97
Zurlo A., et al., 2016, A&A, 587, A57

APPENDIX A: TABLES

In the following Tables are shown the detection probabilities and physical properties (semimajor-axis and mass ratio) for satellites around the 38 planets and brown dwarfs considered in the sample. In Table A1 values are given for the *binary-like* satellite population and in Table A2 for the *planet-like* population. In each column, from left to right, are listed the name of the planet/BD, the detection technique analyzed, the detection probability, the mean, minimum and maximum semi-major axes, and the mean, minumum and maximum mass ratios for detectable satellites, respectively.

This paper has been typeset from a TEX/LATEX file prepared by the author.

Table A1. Detection probability and detected satellite parameters for the binary-like satellite population.

Planet	Method	Prob	$a_{\rm med}$	$a_{\rm min}$	$a_{\rm max}$	$q_{\rm med}$	$q_{\rm min}$	$q_{\rm max}$
1RXS J160929.1-210524 b	Astro	0.1355	0.4776	0.0013	1.8559	0.5580	0.0109	1.0000
1RXS J160929.1-210524 b	RV	0.1301	0.4684	0.0013	1.8559	0.5588	0.0109	1.0000
1RXS J160929.1-210524 b	Transit	0.0119	0.0247	0.0013	0.0537	0.4628	0.0119	1.0000
1RXS J160929.1-210524 b	Imaging	0.1460	8.7624	2.7933	22.6457	0.6975	0.4007	1.0000
2M1207 b	Astro	0.1406	0.4411	0.0013	1.5860	0.5268	0.0100	1.0000
2M1207 b	RV	0.1297	0.4322	0.0013	1.5860	0.5285	0.0100	1.0000
2M1207 b	Transit	0.0100	0.0215	0.0013	0.0462	0.4659	0.0189	0.9999
2M1207 b	Imaging	0.07745	3.2889	1.0483	8.0126	0.7970	0.6040	1.0000
51 Eri b	Astro	0.0708	0.2232	0.0013	0.4938	0.4855	0.0183	1.0000
51 Eri b	RV	0.0000	0.0017	0.0013	0.0035	0.8701	0.6850	0.9920
51 Eri b	Transit	0.0089	0.0191	0.0013	0.0412	0.4690	0.0260	0.9999
51 Eri b	Imaging	0.0000	0.0000	0.0000	0.0000	0.0000	0.0000	0.0000
AB Pic b	Astro	0.1750	0.5908	0.0013	2.2369	0.4952	0.0100	1.0000
AB Pic b	RV	0.1709	0.5875	0.0013	2.2369	0.4955	0.0100	1.0000
AB Pic b	Transit	0.0144	0.0294	0.0013	0.0651	0.4522	0.0100	0.9999
AB Pic b	Imaging	0.1626	5.9725	1.0025	23.7721	0.7507	0.4999	1.0000
beta Pic b	Astro	0.0915	0.2373	0.0013	0.6502	0.4653	0.0100	1.0000
beta Pic b	RV	0.0911	0.2372	0.0013	0.6502	0.4654	0.0100	1.0000
beta Pic b	Transit	0.0135	0.0283	0.0013	0.0617	0.4561	0.0100	0.9999
beta Pic b	Imaging	0.0102	0.5145	0.3888	0.6502	0.7936	0.5883	1.0000
CT Cha b	Astro	0.1471	0.8536	0.0585	2.2854	0.5368	0.0317	1.0000
CT Cha b	RV	0.1759	0.8144	0.0013	2.2854	0.5302	0.0102	1.0000
CT Cha b	Transit	0.0146	0.0297	0.0013	0.0665	0.4495	0.0100	0.9999
CT Cha b	Imaging	0.2785	14.7405	3.8388	47.3395	0.5461	0.1330	1.0000
DH Tau B	Astro	0.1453	0.7422	0.0413	2.0343	0.5242	0.0253	1.0000
DH Tau B	RV	0.1641	0.7207	0.0013	2.0343	0.5204	0.0102	1.0000
DH Tau B	Transit	0.0133	0.0268	0.0013	0.0594	0.4549	0.0100	0.9997
DH Tau B	Imaging	0.3029	13.1787	2.7064	52.1904	0.5705	0.1882	1.0000
eta Tel B	Astro	0.2210	0.9666	0.0024	3.3369	0.4734	0.0100	1.0000
eta Tel B	RV	0.2291	0.9621	0.0013	3.3369	0.4727	0.0100	1.0000
eta Tel B	Transit	0.0188	0.0384	0.0013	0.0971	0.4505	0.0100	0.9999
eta Tel B	Imaging	0.2693	5.6070	0.9474	19.2398	0.5713	0.1624	1.0000
GJ504 b	Astro	0.2040	0.7500	0.0055	2.6347	0.4575	0.0100	1.0000
GJ504 b	RV	0.0000	0.0000	0.0000	2.6347	0.0000	0.0000	1.0000
GJ504 b	Transit	0.0165	0.0331	0.0013	0.0767	0.4442	0.0100	1.0000
GJ504 b	Imaging	0.0000	0.0000	0.0000	0.0000	0.0000	0.0000	0.0000
GQ Lup b	Astro	0.1770	0.9696	0.0458	2.8819	0.5160	0.0200	1.0000
GQ Lup b	RV	0.2100	0.9343	0.0013	2.8819	0.5086	0.0100	1.0000
GQ Lup b	Transit	0.0173	0.0351	0.0013	0.0839	0.4498	0.0100	0.9999
GQ Lup b	Imaging	0.1474	6.5694	3.0349	12.4799	0.5440	0.1159	1.0000
HD1160 c	Astro	0.2134	1.1533	0.0379	3.7470	0.4991	0.0128	1.0000
HD1160 c	RV	0.2391	1.1272	0.0014	3.7470	0.4952	0.0100	1.0000
HD1160 c	Transit	0.0200	0.0407	0.0013	0.1090	0.4404	0.0100	1.0000
HD1160 c	Imaging	0.1478	5.5738	2.5189	10.8196	0.5437	0.1330	1.0000
HD4747 B	Astro	0.1701	0.5899	0.0060	1.7127	0.4471	0.0100	1.0000
HD4747 B	RV	0.1732	0.5890	0.0018	1.7127	0.4469	0.0100	1.0000
HD4747 B	Transit	0.0198	0.0411	0.0013	0.1113	0.4413	0.0100	1.0000
HD4747 B	Imaging	0.0096	0.9684	0.3850	1.7127	0.9459	0.8767	1.0000

Table A1. Cont.

Planet	Method	Prob	$a_{\rm med}$	$a_{\rm min}$	$a_{\rm max}$	$q_{\rm med}$	$q_{\rm min}$	$q_{\rm max}$
HD19467 B	Astro	0.2436	1.0453	0.0015	3.8957	0.4644	0.0100	1.0000
HD19467 B	RV	0.2441	1.0451	0.0014	3.8957	0.4644	0.0100	1.0000
HD19467 B	Transit	0.0204	0.0408	0.0013	0.1131	0.4410	0.0100	0.9999
HD19467 B	Imaging	0.0643	2.4891	0.6407	6.5292	0.8361	0.6773	1.0000
HD72946 B	Astro	0.1160	0.3747	0.0079	0.9423	0.4616	0.0100	1.0000
HD72946 B	RV	0.1243	0.3719	0.0014	0.9423	0.4597	0.0100	1.0000
HD72946 B	Transit	0.0203	0.0408	0.0013	0.1119	0.4476	0.0100	1.0000
HD72946 B	Imaging	0.0034	0.7204	0.5178	0.9422	0.9476	0.8937	0.9999
HD95086 b	Astro	0.1295	0.5609	0.0013	1.5295	0.5133	0.0217	1.0000
HD95086 b	RV	0.0000	0.0014	0.0013	0.0023	0.9384	0.7992	0.9961
HD95086 b	Transit	0.0097	0.0209	0.0013	0.0443	0.4602	0.0210	0.9998
HD95086 b	Imaging	0.0000	0.0000	0.0000	0.0000	0.0000	0.0000	0.0000
HR2562 B	Astro	0.1853	0.5966	0.0013	2.0906	0.5142	0.0100	1.0000
HR2562 B	RV	0.1566	0.5729	0.0013	2.0906	0.5236	0.0101	1.0000
HR2562 B	Transit	0.0172	0.0351	0.0013	0.0831	0.4419	0.0100	1.0000
HR2562 B	Imaging	0.0000	0.0000	0.0000	0.0000	0.0000	0.0000	0.0000
HR3549 B	Astro	0.2079	0.7957	0.0013	3.3702	0.5110	0.0102	1.0000
HR3549 B	RV	0.2015	0.7885	0.0013	3.3702	0.5116	0.0102	1.0000
HR3549 B	Transit	0.0190	0.0383	0.0013	0.0983	0.4423	0.0100	1.0000
HR3549 B	Imaging	0.0798	4.2501	1.9066	8.1100	0.7312	0.4601	1.0000
HR8799 b	Astro	0.1489	0.4253	0.0013	1.6633	0.5731	0.0100	1.0000
HR8799 b	RV	0.0374	0.1629	0.0013	1.3903	0.7642	0.0584	1.0000
HR8799 b	Transit	0.0102	0.0227	0.0013	0.0486	0.4619	0.0163	0.9998
HR8799 b	Imaging	0.0000	0.0000	0.0000	0.0000	0.0000	0.0000	0.0000
HR8799 c	Astro	0.1575	0.4743	0.0013	1.8245	0.5803	0.0100	1.0000
HR8799 c	RV	0.1063	0.4161	0.0013	1.8245	0.6182	0.0200	1.0000
HR8799 c	Transit	0.0117	0.0240	0.0013	0.0530	0.4597	0.0125	0.9998
HR8799 c	Imaging	0.0064	1.5089	0.8261	2.4656	0.9606	0.9208	1.0000
HR8799 d	Astro	0.1596	0.4937	0.0013	1.6995	0.5327	0.0100	1.0000
HR8799 d	RV	0.1317	0.4693	0.0013	1.6995	0.5437	0.0103	1.0000
HR8799 d	Transit	0.0126	0.0261	0.0013	0.0564	0.4589	0.0104	0.9999
HR8799 d	Imaging	0.0121	1.2168	0.8258	1.6995	0.8792	0.7607	1.0000
HR8799 e	Astro	0.1124	0.3137	0.0013	0.9663	0.5621	0.0131	0.9999
HR8799 e	RV	0.0832	0.2844	0.0013	0.9663	0.5865	0.0199	0.9999
HR8799 e	Transit	0.0117	0.0246	0.0013	0.0530	0.4591	0.0125	0.9999
HR8799 e	Imaging	0.0007	0.8959	0.8258	0.9663	0.9593	0.9209	1.0000
HIP64892 B	Astro	0.1866	0.9721	0.0063	2.9754	0.5065	0.0151	1.0000
HIP64892 B	RV	0.1917	0.9656	0.0013	2.9754	0.5065	0.0140	1.0000
HIP64892 B	Transit	0.0178	0.0361	0.0013	0.0870	0.4397	0.0100	0.9998
HIP64892 B	Imaging	0.1297	6.2910	2.5032	13.3070	0.6611	0.3108	1.0000
HIP65426 b	Astro	0.1415	0.5756	0.0013	1.8545	0.5580	0.0225	1.0000
HIP65426 b	RV	0.0163	0.0698	0.0013	0.4690	0.7860	0.0968	1.0000
HIP65426 b	Transit	0.0120	0.0249	0.0013	0.0540	0.4626	0.0120	1.0000
HIP65426 b	Imaging	0.0000	0.0000	0.0000	0.0000	0.0000	0.0000	0.0000
HIP74865 B	Astro	0.1834	0.9444	0.0219	2.5711	0.4881	0.0146	1.0000
HIP74865 B	RV	0.1971	0.9305	0.0014	2.5711	0.4869	0.0106	1.0000
HIP74865 B	Transit	0.0188	0.0380	0.0013	0.0965	0.4445	0.0100	0.9999
HIP74865 B	Imaging	0.0027	2.5187	2.4692	2.5711	0.6367	0.3170	0.9999

Table A1. Cont.

Planet	Method	Prob	a_{med}	a_{min}	a_{max}	q_{med}	q_{min}	q_{max}
HIP78530 B	Astro	0.1656	0.6080	0.0013	2.5114	0.5767	0.0113	1.0000
HIP78530 B	RV	0.1385	0.5557	0.0013	2.5114	0.5867	0.0113	1.0000
HIP78530 B	Transit	0.0160	0.0319	0.0013	0.0728	0.4495	0.0100	1.0000
HIP78530 B	Imaging	0.1251	11.1579	2.7473	38.5397	0.7941	0.5982	1.0000
HIP79098 B	Astro	0.1640	0.8773	0.0176	2.5140	0.5180	0.0222	1.0000
HIP79098 B	RV	0.1871	0.8528	0.0013	2.5140	0.5136	0.0103	1.0000
HIP79098 B	Transit	0.0157	0.0322	0.0013	0.0732	0.4521	0.0100	1.0000
HIP79098 B	Imaging	0.1861	8.7350	2.9283	20.4640	0.5911	0.1748	1.0000
HIP107412 B	Astro	0.1286	0.3761	0.0013	1.1828	0.5176	0.0113	1.0000
HIP107412 B	RV	0.1145	0.3651	0.0013	1.1828	0.5225	0.0113	1.0000
HIP107412 B	Transit	0.0167	0.0340	0.0013	0.0788	0.4482	0.0100	0.9999
HIP107412 B	Imaging	0.0000	0.0000	0.0000	0.0000	0.0000	0.0000	0.0000
k And b	Astro	0.1876	0.7810	0.0056	2.5184	0.4798	0.0100	1.0000
k And b	RV	0.1921	0.7775	0.0016	2.5184	0.4796	0.0100	1.0000
k And b	Transit	0.0157	0.0321	0.0013	0.0733	0.4493	0.0100	0.9999
k And b	Imaging	0.1161	3.1716	1.0000	7.0012	0.6800	0.3500	1.0000
PDS 70 b	Astro	0.1247	0.5885	0.0023	1.3972	0.5092	0.0249	1.0000
PDS 70 b	RV	0.1360	0.5760	0.0014	1.3972	0.5072	0.0102	1.0000
PDS 70 b	Transit	0.0118	0.0249	0.0013	0.0539	0.4615	0.0121	0.9999
PDS 70 b	Imaging	0.0000	0.0000	0.0000	0.0000	0.0000	0.0000	0.0000
PDS 70 c	Astro	0.1391	0.6691	0.0344	1.8374	0.5217	0.0239	1.0000
PDS 70 c	RV	0.1485	0.6596	0.0015	1.8374	0.5208	0.0158	1.0000
PDS 70 c	Transit	0.0117	0.0248	0.0013	0.0536	0.4538	0.0122	0.9998
PDS 70 c	Imaging	0.0008	2.2825	2.2677	2.2980	0.6878	0.3886	0.9997
PZ Tel B	Astro	0.2241	0.9882	0.0144	3.4626	0.4718	0.0100	1.0000
PZ Tel B	RV	0.2328	0.9846	0.0014	3.4626	0.4715	0.0100	1.0000
PZ Tel B	Transit	0.0194	0.0389	0.0013	0.1008	0.4413	0.0100	0.9999
PZ Tel B	Imaging	0.1947	3.7262	0.9426	9.5023	0.5671	0.1500	1.0000
TYC 7084-794-1 B	Astro	0.2141	0.7346	0.0013	2.9407	0.4858	0.0100	1.0000
TYC 7084-794-1 B	RV	0.2005	0.7292	0.0013	2.9407	0.4876	0.0100	1.0000
TYC 7084-794-1 B	Transit	0.0174	0.0358	0.0013	0.0857	0.4465	0.0100	0.9999
TYC 7084-794-1 B	Imaging	0.0990	2.8320	0.4482	9.2910	0.8078	0.6235	1.0000
TYC 8047-232-1 B	Astro	0.1640	0.5727	0.0013	2.2259	0.5285	0.0102	1.0000
TYC 8047-232-1 B	RV	0.1557	0.5628	0.0013	2.2259	0.5298	0.0102	1.0000
TYC 8047-232-1 B	Transit	0.0142	0.0295	0.0013	0.0648	0.4587	0.0100	1.0000
TYC 8047-232-1 B	Imaging	0.1445	7.6613	1.7257	24.6086	0.7510	0.5071	1.0000
TYC 8998-760-1 b	Astro	0.1631	0.5560	0.0013	2.2309	0.5779	0.0108	1.0000
TYC 8998-760-1 b	RV	0.1281	0.5035	0.0013	2.2309	0.5947	0.0108	1.0000
TYC 8998-760-1 b	Transit	0.0144	0.0299	0.0013	0.0651	0.4577	0.0100	1.0000
TYC 8998-760-1 b	Imaging	0.0751	5.5391	1.8922	13.5359	0.8207	0.6451	1.0000
TYC 8998-760-1 c	Astro	0.1353	0.5960	0.0013	1.6837	0.5244	0.0213	1.0000
TYC 8998-760-1 c	RV	0.0028	0.0158	0.0013	0.0734	0.8173	0.1969	0.9998
TYC 8998-760-1 c	Transit	0.0106	0.0229	0.0013	0.0489	0.4611	0.0158	0.9998
TYC 8998-760-1 c	Imaging	0.0000	0.0000	0.0000	0.0000	0.0000	0.0000	0.0000

Table A1. Cont.

Planet	Method	Prob	a_{med}	a_{min}	a_{max}	q_{med}	q_{min}	q_{max}
TYC 8984-2245-1 b	Astro	0.1339	0.6184	0.0013	1.7118	0.5281	0.0243	1.0000
TYC 8984-2245-1 b	RV	0.0023	0.0140	0.0013	0.0600	0.8245	0.2254	1.0000
TYC 8984-2245-1 b	Transit	0.0108	0.0233	0.0013	0.0499	0.4660	0.0151	1.0000
TYC 8984-2245-1 b	Imaging	0.0000	0.0000	0.0000	0.0000	0.0000	0.0000	0.0000
GSC 6214-210 B	Astro	0.1599	0.7707	0.0116	2.2332	0.5129	0.0184	1.0000
GSC 6214-210 B	RV	0.1732	0.7571	0.0013	2.2332	0.5116	0.0101	1.0000
GSC 6214-210 B	Transit	0.0144	0.0291	0.0013	0.0648	0.4501	0.0100	0.9996
GSC 6214-210 B	Imaging	0.1979	7.8972	2.1763	20.7695	0.6121	0.2158	1.0000

Table A2. Detection probability and detected satellite parameters for the planet-like satellite population

Planet	Method	Prob	$a_{\rm med}$	$a_{\rm min}$	$a_{\rm max}$	$q_{\rm med}$	$q_{\rm min}$	$q_{\rm max}$
1RXS J160929.1-210524 b	Astro	0.0003	0.6642	0.0766	1.4529	0.1137	0.0318	0.8339
1RXS J160929.1-210524 b	RV	0.0007	0.1329	0.0045	1.4529	0.1042	0.0188	0.8339
1RXS J160929.1-210524 b	Transit	0.0010	0.0288	0.0045	0.0482	0.0206	0.0119	0.4809
1RXS J160929.1-210524 b	Imaging	0.0000	0.0000	0.0000	0.0000	0.0000	0.0000	0.0000
2M1207 b	Astro	0.0007	0.4628	0.0331	1.2648	0.0719	0.0144	0.9632
2M1207 b	RV	0.0014	0.1739	0.0018	1.2648	0.0629	0.0069	0.9632
2M1207 b	Transit	0.0007	0.0227	0.0031	0.0393	0.0310	0.0189	0.6671
2M1207 b	Imaging	0.0000	0.0000	0.0000	0.0000	0.0000	0.0000	0.0000
51 Eri b	Astro	0.0008	0.2433	0.0285	0.4934	0.0669	0.0188	0.7197
51 Eri b	RV	0.0000	0.0000	0.0000	0.4934	0.0000	0.0000	0.7197
51 Eri b	Transit	0.0006	0.0193	0.0027	0.0345	0.0501	0.0263	0.5353
51 Eri b	Imaging	0.0000	0.0000	0.0000	0.0000	0.0000	0.0000	0.0000
AB Pic b	Astro	0.0018	0.7811	0.0515	1.7940	0.0402	0.0086	0.9798
AB Pic b	RV	0.0025	0.5842	0.0017	1.7940	0.0411	0.0031	0.9798
AB Pic b	Transit	0.0015	0.0326	0.0039	0.0524	0.0117	0.0069	0.9680
AB Pic b	Imaging	0.0000	1.1028	1.1028	1.1028	0.7494	0.7494	0.7494
beta Pic b	Astro	0.0025	0.3304	0.0053	0.6499	0.0319	0.0068	0.8908
beta Pic b	RV	0.0026	0.3172	0.0027	0.6499	0.0317	0.0038	0.8908
beta Pic b	Transit	0.0015	0.0310	0.0026	0.0503	0.0149	0.0081	0.4421
beta Pic b	Imaging	0.0000	0.4887	0.4887	0.4887	0.8851	0.8851	0.8851
CT Cha b	Astro	0.0003	0.8110	0.0876	1.8280	0.1479	0.0373	0.9598
CT Cha b	RV	0.0029	0.1345	0.0025	1.8280	0.0401	0.0039	0.9598
CT Cha b	Transit	0.0016	0.0361	0.0050	0.0536	0.0101	0.0064	0.7438
CT Cha b	Imaging	0.0000	4.4704	4.4704	4.4704	0.1642	0.1642	0.1642
DH Tau B	Astro	0.0004	0.7887	0.0719	1.6682	0.0969	0.0286	0.9005
DH Tau B	RV	0.0030	0.0987	0.0014	1.6682	0.0386	0.0023	0.9005
DH Tau B	Transit	0.0014	0.0302	0.0022	0.0489	0.0142	0.0090	0.4918
DH Tau B	Imaging	0.0000	0.0000	0.0000	0.0000	0.0000	0.0000	0.0000
eta Tel B	Astro	0.0042	1.3311	0.0161	2.8452	0.0229	0.0058	0.9857
eta Tel B	RV	0.0074	0.7237	0.0069	2.8452	0.0196	0.0020	0.9857
eta Tel B	Transit	0.0025	0.0484	0.0069	0.0776	0.0037	0.0021	0.3194
eta Tel B	Imaging	0.0001	1.9034	1.0727	7.3961	0.2405	0.1518	0.9179
GJ504 b	Astro	0.0097	1.0044	0.0474	2.0976	0.0108	0.0026	0.9744
GJ504 b	RV	0.0000	0.0000	0.0000	2.0976	0.0000	0.0000	0.9744
GJ504 b	Transit	0.0021	0.0395	0.0028	0.0659	0.0074	0.0042	0.7005
GJ504 b	Imaging	0.0000	0.0000	0.0000	0.0000	0.0000	0.0000	0.0000
GQ Lup b	Astro	0.0007	1.1754	0.1002	2.3452	0.0911	0.0222	0.8262
GQ Lup b	RV	0.0068	0.2008	0.0037	2.3452	0.0201	0.0016	0.8262
GQ Lup b	Transit	0.0023	0.0422	0.0037	0.0707	0.0059	0.0032	0.6655
GQ Lup b	Imaging	0.0001	4.5483	3.0922	7.0493	0.1394	0.0749	0.3595
HD1160 c	Astro	0.0015	1.5972	0.1798	3.0170	0.0475	0.0132	0.9914
HD1160 c	RV	0.0049	0.5412	0.0060	3.0170	0.0292	0.0021	0.9914
HD1160 c	Transit	0.0025	0.0535	0.0060	0.0872	0.0027	0.0015	0.2191
HD1160 c	Imaging	0.0001	4.1521	2.6365	10.1996	0.2113	0.1137	0.6229
HD4747 B	Astro	0.0092	0.4226	0.0096	1.7120	0.0145	0.0018	0.8484
HD4747 B	RV	0.0070	0.2987	0.0096	1.7118	0.0152	0.0018	0.8484
HD4747 B	Transit	0.0025	0.0538	0.0096	0.0888	0.0027	0.0014	0.2231
HD4747 B	Imaging	0.0000	0.0000	0.0000	0.0000	0.0000	0.0000	0.0000

Table A2. Cont.

Planet	Method	Prob	a_{med}	a_{min}	a_{max}	q_{med}	q_{min}	q_{max}
HD19467 B	Astro	0.0097	0.9089	0.0054	3.5646	0.0166	0.0020	0.9293
HD19467 B	RV	0.0051	0.3409	0.0054	3.5646	0.0217	0.0020	0.9293
HD19467 B	Transit	0.0027	0.0545	0.0054	0.0902	0.0024	0.0013	0.1776
HD19467 B	Imaging	0.0000	1.3402	0.7194	3.1137	0.7971	0.7304	0.9293
HD72946 B	Astro	0.0026	0.6255	0.0596	0.9386	0.0246	0.0083	0.9814
HD72946 B	RV	0.0061	0.4159	0.0144	0.9386	0.0174	0.0018	0.9814
HD72946 B	Transit	0.0026	0.0554	0.0067	0.0899	0.0025	0.0014	0.2643
HD72946 B	Imaging	0.0000	0.0000	0.0000	0.0000	0.0000	0.0000	0.0000
HD95086 b	Astro	0.0004	0.4773	0.0546	1.2067	0.1146	0.0242	0.9472
HD95086 b	RV	0.0000	0.0000	0.0000	1.2067	0.0000	0.0000	0.9472
HD95086 b	Transit	0.0007	0.0238	0.0028	0.0363	0.0345	0.0210	0.4676
HD95086 b	Imaging	0.0000	0.0000	0.0000	0.0000	0.0000	0.0000	0.0000
HR2562 B	Astro	0.0043	0.9190	0.0064	2.0856	0.0258	0.0053	0.9382
HR2562 B	RV	0.0007	0.1957	0.0064	1.9036	0.1112	0.0136	0.9382
HR2562 B	Transit	0.0021	0.0422	0.0044	0.0685	0.0059	0.0034	0.3361
HR2562 B	Imaging	0.0000	0.0000	0.0000	0.0000	0.0000	0.0000	0.0000
HR3549 B	Astro	0.0017	0.7073	0.0078	2.7002	0.0593	0.0071	0.9044
HR3549 B	RV	0.0009	0.2998	0.0078	2.6890	0.0705	0.0071	0.9044
HR3549 B	Transit	0.0024	0.0489	0.0066	0.0795	0.0037	0.0021	0.9044
HR3549 B	Imaging	0.0000	2.2563	2.2563	2.2563	0.6777	0.6777	0.6777
HR8799 b	Astro	0.0012	0.4413	0.0145	1.3470	0.0613	0.0099	0.8706
HR8799 b	RV	0.0001	0.0622	0.0145	0.8883	0.4220	0.2438	0.8706
HR8799 b	Transit	0.0008	0.0237	0.0032	0.0416	0.0284	0.0163	0.3968
HR8799 b	Imaging	0.0000	0.0000	0.0000	0.0000	0.0000	0.0000	0.0000
HR8799 c	Astro	0.0015	0.4562	0.0050	1.4528	0.0569	0.0093	0.9328
HR8799 c	RV	0.0003	0.0646	0.0050	1.3785	0.1704	0.0322	0.9328
HR8799 c	Transit	0.0011	0.0268	0.0016	0.0478	0.0215	0.0125	0.7489
HR8799 c	Imaging	0.0000	0.0000	0.0000	0.0000	0.0000	0.0000	0.0000
HR8799 d	Astro	0.0016	0.2950	0.0023	1.5246	0.0652	0.0096	0.7830
HR8799 d	RV	0.0008	0.0829	0.0023	1.5193	0.0955	0.0115	0.7830
HR8799 d	Transit	0.0012	0.0292	0.0023	0.0454	0.0175	0.0104	0.6983
HR8799 d	Imaging	0.0000	0.0000	0.0000	0.0000	0.0000	0.0000	0.0000
HR8799 e	Astro	0.0011	0.2809	0.0033	0.9655	0.0856	0.0148	0.9761
HR8799 e	RV	0.0003	0.0483	0.0033	0.6771	0.1585	0.0261	0.9761
HR8799 e	Transit	0.0011	0.0266	0.0016	0.0430	0.0218	0.0125	0.3804
HR8799 e	Imaging	0.0000	0.0000	0.0000	0.0000	0.0000	0.0000	0.0000
HIP64892 B	Astro	0.0011	1.1176	0.1003	2.4059	0.0675	0.0173	0.9812
HIP64892 B	RV	0.0014	0.8706	0.0057	2.4059	0.0675	0.0099	0.9812
HIP64892 B	Transit	0.0022	0.0452	0.0039	0.0698	0.0051	0.0030	0.4231
HIP64892 B	Imaging	0.0000	3.1587	3.1587	3.1587	0.5464	0.5464	0.5464
HIP65426 b	Astro	0.0004	0.5805	0.0091	1.4902	0.1017	0.0233	0.9490
HIP65426 b	RV	0.0000	0.0298	0.0091	0.2000	0.8233	0.3292	0.9490
HIP65426 b	Transit	0.0012	0.0250	0.0037	0.0456	0.0209	0.0119	0.9490
HIP65426 b	Imaging	0.0000	0.0000	0.0000	0.0000	0.0000	0.0000	0.0000
HIP74865 B	Astro	0.0011	1.3315	0.0062	2.5680	0.0519	0.0064	0.7037
HIP74865 B	RV	0.0017	0.8260	0.0062	2.5680	0.0464	0.0064	0.7037
HIP74865 B	Transit	0.0026	0.0483	0.0062	0.0819	0.0039	0.0021	0.6502
HIP74865 B	Imaging	0.0000	0.0000	0.0000	0.0000	0.0000	0.0000	0.0000

Table A2. Cont.

Planet	Method	Prob	a_{med}	a_{min}	a_{max}	q_{med}	q_{min}	q_{max}
HIP78530 B	Astro	0.0006	0.3904	0.0066	2.0145	0.1301	0.0227	0.9802
HIP78530 B	RV	0.0003	0.1168	0.0066	1.6370	0.1598	0.0237	0.9802
HIP78530 B	Transit	0.0019	0.0373	0.0022	0.0591	0.0088	0.0049	0.9802
HIP78530 B	Imaging	0.0000	0.0000	0.0000	0.0000	0.0000	0.0000	0.0000
HIP79098 B	Astro	0.0005	1.0176	0.1077	2.0257	0.0856	0.0228	0.7593
HIP79098 B	RV	0.0031	0.1674	0.0028	2.0257	0.0346	0.0026	0.7593
HIP79098 B	Transit	0.0019	0.0382	0.0035	0.0606	0.0081	0.0048	0.2713
HIP79098 B	Imaging	0.0000	6.1033	6.1033	6.1033	0.2104	0.2104	0.2104
HIP107412 B	Astro	0.0020	0.4902	0.0095	1.1827	0.0575	0.0110	0.9275
HIP107412 B	RV	0.0006	0.1436	0.0095	1.0808	0.1183	0.0160	0.9275
HIP107412 B	Transit	0.0020	0.0401	0.0039	0.0645	0.0071	0.0039	0.4704
HIP107412 B	Imaging	0.0000	0.0000	0.0000	0.0000	0.0000	0.0000	0.0000
k And b	Astro	0.0023	0.9059	0.0238	2.3888	0.0360	0.0076	0.9282
k And b	RV	0.0051	0.3595	0.0046	2.3888	0.0278	0.0022	0.9282
k And b	Transit	0.0019	0.0367	0.0034	0.0623	0.0082	0.0048	0.7630
k And b	Imaging	0.0000	1.9240	1.0507	4.3007	0.6422	0.4013	0.9282
PDS 70 b	Astro	0.0004	0.5038	0.0517	1.3935	0.1124	0.0285	0.9115
PDS 70 b	RV	0.0019	0.0963	0.0023	1.3935	0.0567	0.0060	0.9115
PDS 70 b	Transit	0.0009	0.0260	0.0023	0.0517	0.0202	0.0121	0.7725
PDS 70 b	Imaging	0.0000	0.0000	0.0000	0.0000	0.0000	0.0000	0.0000
PDS 70 c	Astro	0.0004	0.6498	0.0662	1.4270	0.0874	0.0273	0.7567
PDS 70 c	RV	0.0020	0.0874	0.0014	1.4270	0.0527	0.0046	0.7567
PDS 70 c	Transit	0.0010	0.0274	0.0020	0.0441	0.0202	0.0123	0.7547
PDS 70 c	Imaging	0.0000	0.0000	0.0000	0.0000	0.0000	0.0000	0.0000
PZ Tel B	Astro	0.0044	1.3655	0.0529	2.7895	0.0212	0.0055	0.9930
PZ Tel B	RV	0.0076	0.8264	0.0044	2.7895	0.0179	0.0016	0.9930
PZ Tel B	Transit	0.0027	0.0489	0.0062	0.0804	0.0033	0.0019	0.5903
PZ Tel B	Imaging	0.0001	2.4945	0.9779	9.1992	0.2024	0.1360	0.5540
TYC 7084-794-1 B	Astro	0.0090	0.8453	0.0023	2.3515	0.0171	0.0029	0.8821
TYC 7084-794-1 B	RV	0.0024	0.1792	0.0023	2.1956	0.0395	0.0035	0.8821
TYC 7084-794-1 B	Transit	0.0020	0.0422	0.0023	0.0685	0.0055	0.0031	0.2619
TYC 7084-794-1 B	Imaging	0.0000	0.8161	0.4743	1.0038	0.8468	0.6583	0.8719
TYC 8047-232-1 B	Astro	0.0008	0.8079	0.0467	1.7777	0.0625	0.0162	0.9701
TYC 8047-232-1 B	RV	0.0009	0.7175	0.0078	1.7777	0.0626	0.0133	0.9701
TYC 8047-232-1 B	Transit	0.0014	0.0342	0.0034	0.0531	0.0127	0.0070	0.8509
TYC 8047-232-1 B	Imaging	0.0000	3.3906	2.5373	3.3906	0.7998	0.5458	0.7998
TYC 8998-760-1 b	Astro	0.0007	0.4509	0.0050	1.8409	0.0972	0.0175	0.9739
TYC 8998-760-1 b	RV	0.0003	0.0832	0.0050	0.9590	0.1540	0.0192	0.9739
TYC 8998-760-1 b	Transit	0.0015	0.0324	0.0030	0.0520	0.0114	0.0069	0.5541
TYC 8998-760-1 b	Imaging	0.0000	0.0000	0.0000	0.0000	0.0000	0.0000	0.0000
TYC 8998-760-1 c	Astro	0.0004	0.4497	0.0037	1.3363	0.1377	0.0245	0.9764
TYC 8998-760-1 c	RV	0.0000	0.0037	0.0037	0.0037	0.3356	0.3356	0.3356
TYC 8998-760-1 c	Transit	0.0009	0.0245	0.0020	0.0434	0.0280	0.0158	0.8493
TYC 8998-760-1 c	Imaging	0.0000	0.0000	0.0000	0.0000	0.0000	0.0000	0.0000

Table A2. Cont.

Planet	Method	Prob	$a_{\rm med}$	$a_{\rm min}$	$a_{\rm max}$	$q_{\rm med}$	$q_{\rm min}$	$q_{\rm max}$
TYC 8984-2245-1 b	Astro	0.0003	0.5682	0.0181	1.4459	0.1142	0.0276	0.9911
TYC 8984-2245-1 b	RV	0.0000	0.0239	0.0181	0.0239	0.9187	0.7906	0.9187
TYC 8984-2245-1 b	Transit	0.0009	0.0248	0.0030	0.0411	0.0252	0.0150	0.9187
TYC 8984-2245-1 b	Imaging	0.0000	0.0000	0.0000	0.0000	0.0000	0.0000	0.0000
GSC 6214-210 B	Astro	0.0007	0.8113	0.0904	1.7815	0.0824	0.0187	0.9526
GSC 6214-210 B	RV	0.0028	0.1463	0.0014	1.7815	0.0423	0.0026	0.9526
GSC 6214-210 B	Transit	0.0015	0.0334	0.0048	0.0532	0.0118	0.0069	0.3818
GSC 6214-210 B	Imaging	0.0000	4.8535	4.8535	4.8535	0.5487	0.5487	0.5487